Journal Pre-proofs

The Pb-Zn-Ag vein system at Montevecchio-Ingurtosu, southwestern Sardinia, Italy: a summary of previous knowledge and new mineralogical, fluid inclusion, and isotopic data

M. Moroni, S. Naitza, G. Ruggieri, A. Aquino, P. Costagliola, G. De Giudici, S. Caruso, E. Ferrari, M.E. Fiorentini, P. Lattanzi

Please cite this article as: M. Moroni, S. Naitza, G. Ruggieri, A. Aquino, P. Costagliola, G. De Giudici, S. Caruso, E. Ferrari, M.E. Fiorentini, P. Lattanzi, The Pb-Zn-Ag vein system at Montevecchio-Ingurtosu, southwestern Sardinia, Italy: a summary of previous knowledge and new mineralogical, fluid inclusion, and isotopic data, *Ore Geology Reviews* (2019), doi: https://doi.org/10.1016/j.oregeorev.2019.103194
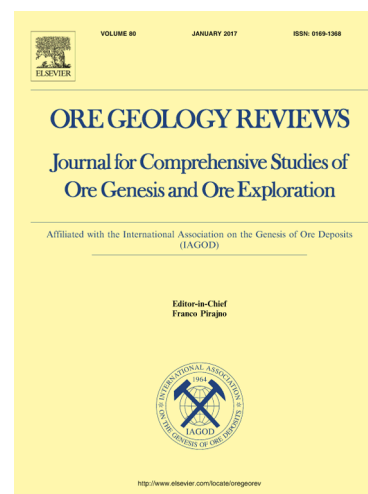
1 The Pb-Zn-Ag vein system at Montevecchio-Ingurtosu, southwestern Sardinia, Italy:

2 a summary of previous knowledge and new mineralogical, fluid inclusion, and

3 isotopic data

4

5   M. Moroni[a], S. Naitza[b,f], G. Ruggieri[c], A. Aquino[d], P. Costagliola[d], G. De

6 Giudici[b], S. Caruso[e], E. Ferrari[a], M.E. Fiorentini[e], P. Lattanzi[c]

7   [a]Dipartimento di Scienze della Terra A. Desio, Università degli Studi di Milano,

8 Italy

9   [b]Dipartimento di Scienze Chimiche e Geologiche, Università degli Studi di

10 Cagliari, Cagliari, Italy

11   [c]IGG-CNR, UOS Firenze, Italy

12   [d]Dipartimento di Scienze della Terra, Università di Firenze, Italy

13   [e]Centre for Exploration Targeting, School of Earth Sciences, University of

14 Western Australia, Australia

15   [f]CNR-Istituto di Geologia Ambientale e Geoingegneria, UOS Cagliari, Cagliari,

16 Italy

17

18   **Abstract**

19   The Montevecchio-Ingurtosu district (SW Sardinia) was among the largest

20 historical Pb-Zn producers of Italy, with significant Ag output, and yields of metallic

21 byproducts such as Cd, Co, Cu, Bi, Sb, Ge, In, and Ga. Despite this importance,

22 detailed descriptions of orebodies and mineral assemblages are surprisingly scarce

23 and old. Here we summarize all previously available information and contribute new

24 textural, microchemical, fluid inclusion, and C-O isotopic data deriving from a recent

25 sampling of currently exposed orebodies. Mineralization occurs as steeply dipping

26 veins extending for almost 20 km at the northern and western flanks of the Variscan

27 Arbus pluton; veins are hosted in phyllites of the Arburese Unit close to the

28 thermometamorphic aureole. Ore enrichments range from massive to coarsely

29 nodular, stockwork and brecciated. Vein filling consists of siderite (locally Zn-rich),

quartz, sphalerite, galena (remarkably rich in micro-inclusions), with accessory chalcopyrite, fahlore, bournonite, barite, and Ni-Co sulfarsenides. Vein assemblages may vary, even within a single vein, from sphalerite- to galena-dominated. Cu-rich assemblages (fahlore+chalcopyrite) were locally observed. Wallrock is affected by silicification, sericitization and pyrite dissemination. Sphalerite shows a complex mineral chemistry, with marked variations in Fe (0.08 to 8.9 mol% FeS) and in Cd contents (from <0.05 to >1 wt%). Trace element analyses (LA-ICP-MS) document the presence of measurable amounts of Ga, Ge, In, Ag, Ni, Co, Tl and Mo. Fahlore varies from the Sb (tetrahedrite) and the As (tennantite) endmembers, with Ag-rich compositions corresponding to Sb endmembers. The occurrence of Cd-rich tetrahedrite (up to 14.5 wt%) is remarkable. Fluid inclusion studies on sphalerite and quartz are in agreement with previous literature data, and indicate comparatively low (in the range 90°-130°C) homogenization temperatures (T_h) and high salinities (14 to 25 equiv. mass % NaCl); both microthermometric data and SEM/EDS analyses of decrepitated inclusions indicate the presence of Ca and K beside Na. Pressure correction to T_h is presumably low (in the order of 10°C), considering a hydrostatic pressure regime. Application of the sphalerite-based GGIMFiS thermometer provided temperatures in excellent agreement with fluid inclusion data for the Montevecchio mineralization. Isotopic data on Montevecchio carbonates define mildy negative $\delta^{13}C_{PDB}$ values (between -1 and -5 per mil), and a larger spread of $\delta^{18}O_{SMOW}$ values, between +14 and +20 per mil. Other isotopic data from literature include a limited set of $\delta^{34}S$ values for galena, sphalerite and pyrite, and a fairly large body of Pb isotopic data on galena. Comparatively narrow ranges for sulfur isotope signatures suggest a homogeneous, possibly igneous, sulfur source, whereas the large spread in Pb isotope signatures reflects the large-scale character of the hydrothermal process and indicates that the Arbus pluton may have been just one of the sources of ore lead. The Montevecchio vein system shows affinities with other late to post Variscan European deposits. The nature of the mineralizing fluids at Montevecchio is analogous to low temperature, basinal brines, and typical of several regional-scale, late to post-

59 Variscan hydrothermal events across Europe. Mineralization at Montevecchio

60 obviously postdates the emplacement of the Arbus plutonic complex, but its exact

61 age remains unknown.

62   .

63

64   **Keywords:** Sardinian metallogeny; Pb-Zn-Ag veins; sphalerite composition;

65 geothermometry; basinal brines

66

67   **1. Introduction**

68   The Montevecchio-Ingurtosu district (shortly, Montevecchio; Arburese region,

69 southwestern Sardinia) was one of the largest Pb-Zn producers of Italy (at least 1.6

70 Mt Pb and 1.1 Mt Zn), with an important Ag output (ca. 1000 t), and a significant

71 yield of other byproduct metals (Cd, Co, Cu, Bi, Sb, Ge, In, and Ga; Rolandi, 1940;

72 Salvadori and Zuffardi, 1973; Carmignani et al., 1994b; and unpublished mining

73 reports). Known at least since Roman times, Montevecchio had its peak of production

74 between 1878 and 1968. Despite this importance, detailed descriptions of the ore

75 bodies and of mineral assemblages are surprisingly scarce and old; the most complete

76 account remains that of Cavinato and Zuffardi (1948). This scarcity of basic

77 geological and mineralogical information is in contrast with existence of a rather

78 conspicuous number of lead isotope data on the Montevecchio ores in literature. On

79 the other hand, there has been recently a revival of studies on the closely associated

80 Arbus pluton and related mineralization (Cuccuru et al., 2016). Moreover, since 1992

81 the district was the subject of extensive studies on the environmental impact and

82 possible reclamation of the abandoned mine wastes (e.g., Sprocati et al., 2013; De

83 Giudici et al., 2014, and references therein). After final closure in 1991, practically

84 all the extensive underground tunnel network became inaccessible. However, today it

85 is still possible to observe mineralized outcrops at some stopes, and/or to collect ore

86 samples in the dumps. In 2013 we had the opportunity of a systematic visit to several

87 accessible outcrops and dumps throughout the district and we collected what we

88 believe is a representative suite of samples, even if biased toward the shallowest

89 portions of the steeply dipping veins. In this contribution, we shall present new

90 textural, microchemical, fluid inclusion and C-O isotopic data, obtained on the new

91 set of samples. By integrating these new data with information from the literature and

92 old mining reports, we provide a picture, admittedly incomplete, of this large district,

93 and we briefly discuss its affinities with other Pb-Zn-Ag vein deposits.

94

95 **2. Background geology**

96 2.1 *Regional geological context*

97 The Arburese region stands in the frontal part of the external nappes of the

98 Variscan basement of Sardinia (Carmignani et al., 1994a; Fig. 1a). In this area two

99 nappe units, the Arburese Unit and the underlying Gerrei Unit, were stacked onto the

100 Variscan Foreland; they consist of Cambrian to Devonian low-grade to very low-

101 grade metamorphic rocks (Barca et al., 1992; Carmignani et al., 1986). In the

102 foreland succession the Gonnesa Formation, a thick early Cambrian carbonatic unit,

103 hosts large MVT Pb-Zn deposits (Boni et al., 1996). The main thrust between nappe

104 and foreland units is low-angle and northward-dipping; where exposed, it is marked

105 by a cataclastic zone, locally >100 m-thick, mainly involving Arburese Unit

106 siliciclastic metasediments and minor calc-alkaline felsic metavolcanics, and tectonic

107 slices of black shales and metalimestones.

108 At 304±4 Ma (U-Pb zircon age; Cuccuru et al., 2016) the metamorphic

109 basement was intruded by the post-collisional Arbus plutonic complex followed by

110 the Monte Linas pluton (289±1 Re-Os age on molybdenite, Boni et al., 2003b) to the

111 south (Fig.1b). The geological and petrological features of the polyphasic Arbus

112 pluton have been outlined by Secchi et al. (1991), Secchi and D'Antonio (1996), and

113 Cuccuru et al. (2016). Swarms of NNE-SSW to NW-SE trending leucogranitic

114 granophyre (quartz-porphyry) dikes intruded the Paleozoic sequences in the western

115 sector. The last magmatic pulse is represented by rare NNE-SSW spessartitic

116 lamprophyre dikes that crosscut the main intrusions and the country rocks. The

117 contact aureole around the Arbus pluton is asymmetric, and its thickness increases

118 from some tens of meters at the northern contact to several hundreds of meters in the

119 south. The late phases of magma emplacement in the Arbus pluton were associated to

120 magmatic fluid production, sub-solidus alteration of granodiorites and development

121 of a magmatic cupola with tourmaline-bearing miarolitic pegmatites and tourmaline-

122 bearing greisens in the northern and western borders of the pluton (Cuccuru et al.,

123 2016; Bosi et al., 2018). After emplacement, the pluton was surrounded and partly

124 dismembered by several fault systems (see the next paragraph), which resulted in

125 northward tilting. After the early Permian, the pluton and the surrounding

126 metamorphic basement underwent repeated erosional phases (late Permian-Triassic,

127 Eocene, Miocene, Pliocene), which dismantled the metamorphic roof and most part

128 of the pegmatitic, greisenized cupola.

129 2.2 *The Montevecchio-Ingurtosu-Gennamari vein system*

130 The Montevecchio-Ingurtosu-Gennamari mine district exploited a narrow

131 swarm of large quartz-siderite and Pb-Zn sulfide veins forming a "peripheral" system

132 (Salvadori and Zuffardi, 1973) that crops out for more than 20 km around the Arbus

133 pluton (Fig. 1c). From NE to SW the main mining sites are Montevecchio (and

134 associated stopes of Levante, Colombi and Centrale Minghetti exploiting the S.

135 Antonio vein system), the Sanna mine area, the Arco di Telle (or Telle) mine area,

136 the Casargiu-Ingurtosu mine area (exploiting the Brassey, Cervo and Ingurtosu vein

137 systems), and the Gennamari mine area. A second, low-mineralized vein system (the

138 so-called "radial" or "intersecting" vein system) cuts across the pluton, with E-W to

139 NW-SE dominant directions, the only exception being the large N-S "Arburese" vein

140 (Fig. 1b-c). A striking feature of the district is the geometrical coherence and

141 continuity of these mineralized fracture fields. The peripheral veins occur as steep,

142 large anastomosing fractures, constantly dipping away from the edge of the pluton

143 and developed 0.5-3 km from the intrusion margins (Fig. 1b). Single veins are up to

144 7-8 m thick, attaining over 20 m of thickness in zones where they merge together.

145 The "radial" veins also attain over 5 m in thickness, and constantly dip northward,

146 again with the exception of the sub-vertical Arburese vein. The northern branch of

147 the "peripheral" system runs N60°E, turning toward N-S in the western sectors, and

148 to NW-SE and E-W in the southern areas, respectively. Veins are thicker, more

149 mineralized and continuous in the northeastern (Montevecchio, with the outstanding

150 S. Antonio vein system) and in the southwestern (Ingurtosu and Gennamari mines)

151 sectors. In the richest veins, mineworks reached a depth of more than 600 m. Beyond

152 the northeastern edge of the pluton, the vein systems are displaced by the Tertiary

153 faults of the Campidano graben (Salvadori, 1958). In the southwestern end, south of

154 Gennamari, the Zn and Pb veins of the S'Acqua Bona and Nieddoris Mines (Fig. 1c)

155 represent the SE extension of the Montevecchio vein system parallel to the granite

156 contact and point towards the historical Southern Arburese mining compound.

157 Besides skarn and Sn-As veins (Naitza et al., 2017), the latter compound is host to a 7

158 km-long, ENE-WSW trending Ni-Co-As-Zn-Pb-Ag vein system (Naitza et al., 2015;

159 Moroni et al., 2019) extending along a tectonic corridor between the Arbus and the

160 Monte Linas intrusions (Fig. 1b). Host rocks of the "peripheral" Montevecchio veins

161 are lower greenschist facies Cambrian-early Ordovician siliciclastic metasediments,

162 and, less commonly, rhyolitic-rhyodacitic metavolcanics ("porphyroids") belonging

163 to the Arburese tectonic unit. The southern branch of the vein system is fully hosted

164 within the Ordovician-Silurian siliciclastic metasediments of the Variscan Foreland.

165 No recent structural studies are available for the area. The fractures might have beeen

166 developed under brittle conditions from the volumetric shrinkage associated with

167 pluton cooling (e.g., Cuccuru et al., 2016, and references therein). However, several

168 old mine reports and the review works by Cavinato and Zuffardi (1948) and Zuffardi

169 (1948) provided a different interpretation of the ore-bearing fracture system: in both

170 Ingurtosu and Montevecchio mine areas the spatial arrangement of veins suggests a

171 definite left-lateral strike-slip component, with highly mineralized zones

172 corresponding to a series of dilational jogs related to main faults. At Ingurtosu and

173 Gennamari, the geometry and the continuity of mineralized bodies are also strongly

174 influenced by numerous intersections with the veins of the "radial" system. The

175 "radial" veins are sulfide-rich close to these intersections, becoming gradually barren

176 inside the Arbus pluton. A precise chronology of the mineralizing events in the

177 district is still unclear, although crosscutting of quartz-porphyry dikes by ore veins

178 were directly observed underground (e.g., Casargiu and Gennamari areas, Wright,

179 1939). Hence, hydrothermal veining took place later than dike emplacement,

180 according to normal to strike-slip faulting and to the "peripheral" and "radial"

181 patterns: at Ingurtosu and Gennamari the two vein systems show mutual crosscutting

182 relationships, so that they should be reasonably considered as contemporaneous.

183   2.3 *Ore textures and mineral assemblages.*

184   The general mineralogical and textural characters of Pb-Zn ores from the

185 Montevecchio vein systems are reported in the classical works of Cavinato and

186 Zuffardi (1948), Zuffardi (1948), Zuffardi (1962), and Salvadori and Zuffardi (1973);

187 on the other hand, the only systematic ore microscopy study of the Ingurtosu and

188 Gennamari deposits is by Dessau (1935). A schematic overview of the geological,

189 textural and mineralogical characters of the main veins of the district as derived from

190 literature is presented in Table 1a attached as Electronic Supplementary Material

191 (ESM).

192   At the macroscopic scale, mineralized veins consist of coarsely crystalline,

193 dominant sphalerite and/or galena which may be concentrated in sulfide-rich shoots

194 over one meter thick, as well as scattered through the siderite-quartz veins and

195 disseminated in the wallrock. The vein filling constantly shows banded and

196 brecciated textures. Banded textures include repeated quartz, siderite and sulfide

197 layers, usually irregular, brecciated and cemented by late sulfides, calcite and barite;

198 cockade textures are also frequent. Brecciated textures including wall rock fragments

199 are common as well, in narrow veins or in zones of intersection of different veins.

200 The contact with the host rocks is marked by thick quartz stockworks and,

201 occasionally, by a clayey gouge (e.g. Ingurtosu mine). Wall rock alteration includes

202 zones of sericitization and silicification of variable intensity. The primary sulfide

203 mineral association mainly consists of sphalerite and galena, with a wide variety of

subordinate minerals: the most abundant are chalcopyrite, fahlore, arsenopyrite, pyrite and argentite. Accessory Ni-Co phases (gersdorffite and ullmannite) are common in the whole mining district; moreover, Ni-Co arsenides (rammelsbergite, skutterudite) were reported in the veins of the southern sector (Nieddoris; Fig. 1c). Gangue minerals include quartz with abundant siderite, ankerite, barite, dolomite and calcite. Galena was often found massive and spathic; it prevailed in the Sant'Antonio (Montevecchio pole) and Ingurtosu veins, where large masses have been described. Sphalerite was abundant in the Sanna vein (Montevecchio pole), and in many of the Casargiu, Ingurtosu and Gennamari veins, occurring in masses and disseminations in quartz and siderite. As a rule, during the mining exploitation sphalerite, as well as pyrite, chalcopyrite, and fahlore, were reported to become more abundant at increasing depths (Rolandi, 1940; Cavinato and Zuffardi, 1948; Zuffardi, 1962). Supergene alteration of primary sulfides produced a wide variety of secondary minerals, including cerussite, anglesite, smithsonite, pyromorphite, goslarite, and hydrozincite. The development of supergene alteration was particularly extensive at the Sanna stope (Zuffardi, 1962). Comprehensive lists of minerals occurring in the district were compiled by Binotto et al. (1987a, b, c; 1988), Stara et al. (1994), Preite and Zuanel (2007); they are summarized in Table 1b ESM.

Due to the extreme variability of textural situations, to the commonly accepted multiphase character of the mineralization (Dessau, 1935; Cavinato and Zuffardi, 1948), and to the scale of the deposits, it was difficult to reconstruct a reliable detailed paragenetic sequence of the ores. Nevertheless, the previous authors had envisaged a very general depositional sequence consisting of: barren quartz → quartz with disseminated sphalerite → massive sphalerite → siderite → massive galena with chalcopyrite, tetrahedrite, and barite → calcite and /or ankerite. However, as detailed below, this is only a broad scheme, with a wide range of variations.

3. Summary of previous geochemical data

3.1 *Bulk ore chemistry*

233   Bulk analyses of ore concentrate (both galena and sphalerite) are available from

234 old mine reports and historical bibliographic sources. Table 2 ESM summarizes the

235 available data for selected accessory elements in galena and sphalerite concentrates.

236 Galena concentrates showed variable contents of Ag, As, Bi and Sb (Bianchini et al.,

237 1960a, b; 1961); specifically, the average silver grade was in the order of 700 g per

238 tonne of Pb (Bianchini et al., 1960a, b; Brigo et al., 1982). The Ag/Pb ratio varied

239 laterally across the district, in relation to variability in mineral assemblages, and was

240 also observed to gradually decrease with depth, in a more rapid way in the uppermost

241 sectors of the deposits compared to the deepest sectors. Bianchini et al. (1960a-b,

242 1961) noted that massive galena shoots may be less Ag-rich than the so-called

243 "mixed ore", represented by relatively fine-grained sphalerite-galena stockworks

244 cementing brecciated wallrock and generally considered least economic. This mixed

245 ore typically occurred in the upper portions of the deposits and is still accessible in

246 various mining sites. Gold, on the other hand, was never regarded as an economic

247 element. There are anecdotal reports, by the former mine staff, of minimal gold

248 production, but there are no explicit statements in the mine files. Bertolio (1909)

249 reports 6 g Au per tonne of galena concentrate for a single small vein at Telle; some

250 1960s analyses yielded up to 0.4 mg Au per kg of galena concentrate.

251   In sphalerite, Fe contents were very variable, ranging from a true "marmatite" in

252 some of the Montevecchio veins, to Fe-poor at Ingurtosu (Zuffardi, 1962); Cd, Co,

253 Ga, Ge and In contents were high enough to warrant recovery of these metals as

254 byproducts (Rimatori, 1904; Stoiber, 1940; Rolandi, 1940; Zuffardi, 1953; Salvadori

255 and Zuffardi, 1973). In particular Zuffardi (1953) reported details about Ga, In, Ge,

256 Tl, Sn and Mo distribution in sphalerite and their distribution with depth of mining

257 (summarized data in Table 2 ESM) while drilling the medium-lower portion of the S.

258 Antonio vein system. Zuffardi invoked the need of additional, accurate investigations

259 on Ge after observing highly variable Ge distribution even within a single lode.

260 Bianchini et al. (1961) also monitored the common occurrence of Ni and Co across

261 the district (up to > 0.005 wt% Co and > 0,015 wt% Ni); these metals appeared to be

262 preferentially associated with sphalerite-rich rather than galena-rich ores (see Table 2
263 ESM).

264

265   3.2 *Isotopic and fluid inclusion data*

266   There is a fair amount of Pb isotope data on Montevecchio, albeit scattered
267 throughout several papers. Most data refer to galena, but there are a few data on
268 feldspars of the Arbus intrusion, and of other Variscan intrusions in Sardinia
269 (Swainbank et al., 1982; Ludwig et al., 1989; Boni et al., 1992; Orgeval et al., 2000).
270 In the context of archaeometallurgical studies, lead isotope data of Montevecchio
271 were reported by Stos-Gale et al. (1995), while a more recent data set was presented
272 by Valera et al. (2005). All data are compiled in Table 3a ESM. Regarding stable
273 isotopes, sulphur isotope data on the mineralized systems are limited to the fifty-year
274 old studies by Brusca et al. (1965) and Jensen & Dessau (1966), who analyzed
275 galena, sphalerite, and single samples of chalcopyrite and pyrite; these data are
276 reported in Table 3b ESM. We also mention the $\delta^{66}Zn$ value of +0.15 per mil
277 reported for two composite sphalerite samples by Wanty et al. (2013). Previous fluid
278 inclusion studies on the Montevecchio district are quite scarce and comprise a crush-
279 and-leach study by Honisch (2008), and few microthermometric data by Boni et al.
280 (2009). These isotopic and thermometric data will be further commented in the
281 Discussion section.

282

283   **4. Sampling and analytical methods**

284   Samples were collected from accessible high-level galleries and mineralized
285 outcrops exposed in open pits and trenches at the following localities (Fig. 1c): the S.
286 Antonio vein system at the Montevecchio, Levante-Colombi and Centrale Minghetti
287 stopes, the Sanna veins near the Sanna mineworks, the Telle veins near the Arco di
288 Telle mineworks, and Gennamari veins at Gennamari and S.Antonio-Pozzo Edoardo
289 mineworks. Samples from the Casargiu veins could only be collected in the mining
290 dumps. Figure 2a-d shows the sampling locations between Montevecchio and Telle in

satellite views (from Google Maps), where the trend of the vein system and its

exposures are best discernible.

A total of 50 hand specimens (listed in Table 4 ESM) were selected for this

study; from these, 43 polished chips and 35 thin sections were obtained and examined

by means of reflected and transmitted light microscopy and by scanning electron

microscope (SEM). Of these sections, 24 were selected for EPMA and 7 for LA-ICP-

MS analysis. Major element microchemical analyses were performed on major and

accessory ore minerals as well as on gangue minerals at the electron microprobe

laboratory of the Earth Science Department, State University of Milano, Italy. At the

IRMS-stable isotope laboratory of the same Department reconnaissance carbon and

oxygen isotope analyses were carried out on carbonates. A further selection of

mineralized samples was subjected to preliminary in-situ trace element analyses on

sphalerite and galena by laser ablation coupled with a quadrupole ICP-MS; these

analyses were performed at the GeoHistory Facility of the John de Laeter Centre,

Curtin University, Perth, Western Australia. Details on the analytical methods for

microchemistry, isotope data acquisition, fluid inclusion analysis, standard materials

and data elaboration are given in the Appendix 1 ESM.

Based on a preliminary inspection of polished and thin sections (see § 5.3),

doubly polished thin sections were prepared from four hand specimens, allowing the

study of inclusions in sphalerite (three samples), and quartz (two fragments from a

single sample; see § 5.6). Fluid inclusion microthermometry was carried out in the

IGG-CNR laboratory at UOS Firenze with a Linkam stage. After completing the

microthermometric study, some samples were thermally decrepitated, and the open

inclusions at the surface were inspected by a Zeiss EVO scanning electron

microscope equipped with an Oxford EDS.

All the geochemical data produced during this study are gathered in tables in the

Electronic Supplementary Material (ESM): major element chemistry of sulphides,

silicates and carbonates in Tables 5a-g, trace element data of sphalerite (and galena)

319   in Tables 5a-e, fluid inclusion data in Table 7a-b, and C-O isotope data of Fe

320   carbonates in Table 8.

321

322   **5. Results**

323   5.1 *Mineral textures: the field scale*

324   Where best visible, mineralization is hosted in multiple, parallel to braided vein

325   structures, with thickness varying between few cm to various meters. Metapelitic and

326   metapsammitic wallrock is moderately silicified and sericitized, with local fine

327   disseminations of pyrite. In agreement with mining reports, wide brecciated zones,

328   rather than sharp, faulted margins characterize the transition from the veins to

329   wallrock. These general field characters can be observed clearly at S. Antonio-

330   Levante/Cantiere Colombi stopes, where several veins of the large S. Antonio system

331   are accessible over a vertical span of about 100 m by means of trenches, adits and

332   shallow galleries, steep cliffs, and a series of parallel paths intersecting the outcrops

333   at different levels (Fig. 2b and 3a). The main mineralized veins are several meters-

334   thick and accompanied by swarms of veinlets of different composition. The

335   orientation of most of the veins roughly conforms to the general ENE-WSW trend of

336   the Montevecchio system north of the Arbus pluton, but single mineralized structures

337   may diverge either by direction or by dip. As an example, the largest vein occupying

338   the central position in the Levante stope (banded to nodular/cockade sphalerite-

339   galena-rich vein) is high-angle (70-80°) and northward dipping, whereas a second

340   galena-quartz-rich vein is much less steep (40-45°), with a southern dip. Analogous

341   geometric relationships between veins are also visible in the outcrops close to the old

342   Sanna mine, where two galena-rich crosscutting veins (here named left-hand and

343   right-hand veins) were sampled (Fig. 2c and 3b). The main Montevecchio orebodies

344   may laterally pass either to poorly mineralized quartz-rich stockworks, or else to

345   plurimetric, parallel swarms of veinlets with massive to brecciated sphalerite

346   cemented by concretionary quartz (like in the Montevecchio Levante stope, Fig. 3b),

347   or to peripheral galena-barite veins (like at the Cantiere Colombi stope and at Telle;

348   Fig. 3c-d). The degree of tectonic disturbance of the mineralization can be variable

349   from site to site. At the Levante stope, mineralized veins are generally affected by

350   late fracturing, but to a much lesser extent compared to, for example, the mineralized

351   outcrops at Sanna (Fig. 3b) or at Arco di Telle.

352   At each visited site, the exposed vein structures commonly show ore and gangue

353   mineral assemblages variably ranging between two endmember assemblages: (1)

354   sphalerite (dominant) + carbonates + quartz, and (2) galena (dominant) ± quartz ±

355   siderite ± barite. The range of mineral assemblages observed in the high-level

356   outcrops bears many similarities with those reported in literature (Dessau, 1935;

357   Cavinato and Zuffardi, 1948; Salvadori and Zuffardi, 1973) for the vertical zoning of

358   the mineralization. The photos in Fig. 4a-g display the textural variability of

359   mineralization in hand specimen from the different mining sites. In the sphalerite-

360   dominated veins (Fig. 4a-b-c-f), both nodular-cockade to crystalline sphalerite and

361   abundant euhedral siderite, plus saccharoidal, transparent to milky to light grey turbid

362   quartz, may intergrow along the axis of cavities and fractures in brecciated, silicified

363   wallrock cemented by quartz. At Montevecchio, sphalerite may also occur as

364   remarkably elongated, parallel to radiated "lamellar" aggregates intergrown with

365   quartz (Fig. 4c) considered by Salvadori and Zuffardi (1973) as parts of coarse-

366   grained sphalerite-barite cockades replaced by quartz. Galena-free sphalerite-siderite

367   vein mineralization was observed in peripheric massive veins at S. Antonio Levante

368   (shown in Fig. 3c), and in some samples derived from the accessible part of the mine

369   dumps at Casargiu. The sphalerite-only Casargiu ore facies (Fig. 4f) displays a

370   characteristic growth of sphalerite and siderite after early vein quartz cementing

371   deeply silicified and sericitized wallrock. When present, galena may be as abundant

372   as sphalerite (and occasionally intergrown with it – Fig. 4b), and occurs as small to

373   large, subhedral crystals and nodules (Fig. 4e) as well as veinlets (Fig. 3e, 4g) in

374   quartz, barite or siderite. Galena-rich vein portions (with minor sphalerite) are

375   common along the S. Antonio and Sanna veins, while the galena-barite-rich samples

376   from Telle (Fig. 3e) and the galena-quartz and galena-siderite-rich samples

377 Gennamari (Fig. 4g) examined in this study appear to be sphalerite-free. An

378 exception to the general assemblage of siderite-rich veins with sphalerite ± galena is

379 represented by the Cu-rich ore facies cropping out at the Centrale Minghetti stope, in

380 the S. Antonio vein system (Fig. 4d). Here, beside abundant galena and sphalerite, the

381 siderite-rich ore breccias in the vein exposures may be enriched in tetrahedrite and

382 locally chalcopyrite, both usually in accessory amounts elsewhere.

383 Pyrite is an infrequent macroscopic component of the mineralization, at least in

384 the inspected parts of the deposits. Fine- to very fine-grained pyrite may be a

385 common accessory phase in the altered wallrock along the veins selvedges, as well as

386 in the deeply altered lithic fragments entrained by the veins.

387 At Casargiu a single sample revealed peculiar, "anomalous" characters with

388 respect to all other samples, possibly linked to a different style of mineralization,

389 herewith labelled Casargiu HT ore facies (HT stands for high temperature, for

390 reasons explained below). Macroscopically, this sample displays the typical

391 brecciated texture with granular to dendritic galena-sphalerite aggregates (Fig. 4h),

392 but microscopic and microchemical inspections (see §5.2 and §5.3) reveal significant

393 differences in mineral assemblages, including the occurrence of Fe-rich sphalerite, K-

394 feldspar (adularia) and fluorite.

395

396 5.2 *Petrographic and microtextural features of ore and gangue minerals and*

397 *wallrock alteration*

398 Microscopic studies of the new samples from the Montevecchio district

399 recognized most of the characters described in earlier studies but previously

400 unreported features were also observed. Overall, ore textures are fairly consistent in

401 all studied samples, both from outcrops and dumps, across the mining district, with

402 the significant exception of the "anomalous" Casargiu HT facies, that will be

403 described separately. Photomicrographs by optical microscopy in Fig. 5, 6, 7 and 8

404 illustrate various features and textures of the observed ore and gangue mineral

405 assemblages. Fig. 9 shows images of ore and gangue minerals obtained by means of

406 scanning electron microscopy (SEM). In Appendix II ESM a brief account is given

407 about supergene alteration features of major ore phases.

408 In order of abundance or frequency the observed ore minerals include:

409 sphalerite, galena, fahlore, chalcopyrite, bournonite, Ni-Co sulfarsenides and pyrite.

410 Coarse-grained sphalerite tends to be moderately transparent and characterized

411 by marked, variable optical zoning [Fig. 5a-b-c, 7b-d-e] as well as by anomalous

412 anisotropy [Fig. 5d], explained by Seal et al. (1985) as due to wurtzite-like stacking

413 domains in Cd-bearing varieties. Sphalerite occasionally contains micro-inclusions of

414 chalcopyrite, fahlore, Ni-Co sulfarsenides (e.g. Fig. 9e) and, exceptionally, gold (Fig.

415 9g).

416 Throughout the district coarse-grained **galena** is ubiquitous; in sphalerite-rich

417 samples galena may also occur as finely disseminated blebs. The most evident

418 feature involves the typical galena cleavage which can be greatly enhanced [Fig. 5e],

419 and locally curved, in response to local post-ore cataclastic deformation (e.g., at the

420 Cantiere Sanna stope, Fig. 4e). Dessau (1935) reported this ductile-fragile

421 deformation in galena as characteristic of the whole district. Another impressive

422 feature in galena is the great amount of inclusions of other major and accessory

423 phases, such as chalcopyrite, fahlore, bournonite, sphalerite, Ni-Co sulfarsenides and

424 native antimony [Fig. 5f, Fig. 6c-d-e, Fig. 8b-d-h]. These inclusions may range all the

425 way between relatively coarse (millimetric to sub-millimetric, e.g., inclusions of

426 chalcopyrite, sphalerite and Ni-Co sulfarsenide crystals) to extremely fine-grained,

427 i.e. sub-micrometric. The most remarkable feature is indeed the almost ubiquitous,

428 dense dissemination of submicrometric blebs and droplets, hardly discernible at the

429 optical microscope, and best detected at high magnification at SEM [Fig. 9b-c-d-h].

430 This feature of the Montevecchio galena is similar to what observed in galenas of the

431 Southern Arburese Ni-Co-As-rich veins (Moroni et al., 2019). Inclusion-rich and

432 inclusion-free zones in galena, possibly related to different stages of deposition, may

433 coexist at the millimetre to centimeter scale (e.g., Fig. 9b). As detailed in Appendix II

434 ESM, galena appears to be the sulphide most affected by weathering.

435   **Fahlore** is the most abundant sulfosalt, associated primarily with galena,

436 chalcopyrite and accessory **bournonite**. Fahlore may constitute most of the fine-

437 grained inclusions in galena. Moreover, in the Cu-rich outcrops of the S. Antonio

438 vein at the Centrale Minghetti site, fahlore, with subordinate bournonite, is among the

439 major components of the mineralization. Here fahlore, inclusion-rich galena and

440 minor sphalerite are variably intergrown with large chalcopyrite aggregates, or else as

441 Cu-rich stockworks locally developing along the cubic cleavage of galena (Fig. 6a-b-

442 c). All these phases are interstitial to the siderite-rich gangue. In these samples

443 coarse-grained fahlore aggregates display slight, but perceivable, optical zoning. This

444 zoning can be detected also by SEM backscattered electron images (Fig. 9c) and

445 corresponds to compositional differences (see § 5.4).

446   In the Montevecchio samples examined in this work, the common accessory **Ni-**

447 **Co phases** are represented by Ni-Co sulfarsenides belonging to the gersdorffite-

448 ullmannite solid solution (see § 5.4). These minerals occur as small, sub-millimetric,

449 isotropic, euhedral bluish/pinkish white crystals disseminated in the quartz gangue in

450 small clusters and occasionally incorporated in nearby coarse galena, fahlore or

451 sphalerite aggregates. The sulfarsenide crystals may show cores made of euhedral

452 As-bearing pyrite [Fig. 6d and 9f]. When occurring as monophasic crystals,

453 sulfarsenides display radial or sector zoning, best evident at SEM (Fig. 9e).

454   The **Casargiu HT** ore facies is characterized by galena, sphalerite and pyrite,

455 with accessory rutile (intergrown with sphalerite), chalcopyrite, pyrrhotite, Ni-Co

456 sulfarsenides, and pyrargyrite. Sphalerite is much less transparent (with red internal

457 reflections) and is affected by "chalcopyrite disease" with abundant drop-like

458 inclusions of chalcopyrite, pyrrhotite, and locally galena (Fig. 6f). Pyrargyrite is the

459 only sulfosalt occasionally included in galena, which is devoid of fahlore. As detailed

460 below, these differences in ore mineral assemblages correspond to differences in

461 gangue minerals as well as sphalerite chemistry.

462   The filling of the Montevecchio veins is dominated by gangue minerals,

463 represented by quartz, carbonates and, subordinately, barite, plus supergene phases

such as cerussite and anglesite. **Quartz** is by far the most frequent gangue mineral, although carbonates may prevail in portions of the veins. Quartz occurs both in the altered, silicified wallrock, in the veins along the selvedges, and in the core of the veins, thereby crystallizing during several stages, and being both older and younger than siderite and sulphides. Some quartz microtextures are illustrated in Fig. 7a-f. Vein quartz may bear abundant dust-like inclusions arranged according to variable growth patterns, often outlining the structure of a preexisting phase completely replaced by late vein quartz. The best example of this texture, shown in Fig. 7e-f, is found in portions of the S. Antonio vein system, where the macroscopic fibrous texture of sphalerite ore (see Fig. 4c) is in fact a ghost texture of a pre-existing radiating aggregate of coarse-grained lamellar crystals (probably barite; Salvadori and Zuffardi, 1973) replaced by crystalline quartz and sphalerite. A similar texture is further documented in the altered and brecciated wallrock of the S. Antonio vein system, where coarse-grained, randomly oriented lamellar ghost crystals were completely replaced by fine-grained mosaic to vuggy quartz, siderite and sphalerite + galena (Fig. 7g-h).

Carbonates represent a major gangue mineral component in the core of most of the veins of the district. Carbonates may prevail over quartz in various portions of the S. Antonio vein system, in the Casargiu-Brassey vein system (in analogy with the major Brassey orebody in the nearby Ingurtosu mining pole), and in some veins at Gennamari. **Siderite** is by far the most abundant carbonate, followed by Zn carbonate and accessory calcite; in our samples, ankerite is very rare. Almost always siderite occurs as aggregates of medium-fine- (sub-mm) (Fig. 7a and h) to, more often, coarse-grained (cm) euhedral to curved, fan-like crystals (Fig. 7b-d), ubiquitously displaying a skeletal, lace-like structure when intergrown with vuggy quartz (Fig. 7c). **Zn carbonate** veinlets may cement late fractures of the siderite aggregates. However, Zn carbonates also occur in unaltered samples (from Centrale Minghetti, Sanna and Casargiu), where vuggy siderite crystals often display either sharp or progressive Zn enrichment along their margins, culminating with the development of rims of Zn

493 carbonate. Occasionally the Zn carbonate-rich rims may also grow thicker and

494 develop independent crystal habits. These textures are best observed by means of

495 SEM imagery, as shown in Fig. 9i-j-k. In samples with such features deposition of

496 quartz and sphalerite followed the crystallization of the siderite-Zn carbonate

497 intergrowths (e.g. Fig.9l). What observed is comparable to Zuffardi's (1962)

498 descriptions of "monheimite" (ferroan smithsonite).

499   The coarse-grained **barite** observed in the peripheral portions of the S. Antonio

500 vein system (e.g., Cantiere Colombi) and at Arco di Telle occurs in typical sheaf-like

501 aggregates with interstitial sulfide-sulfosalt blebs (galena, chalcopyrite, fahlore) and

502 minor quartz.

503   A markedly different gangue mineral assemblage characterizes the Casargiu HT

504 sample. The gangue of the galena-sphalerite mineralization consists of the

505 hydrothermally altered metapelitic wallrock breccia cemented by calcite, quartz,

506 fluorite and lozenge-shaped K-feldspar (adularia), crystals (Fig. 8a-b). Adularia is

507 locally in direct contact with, and incorporated in, sulphides intergrown with gangue

508 in the vein stockwork [Fig. 8a]. The phyllite fragments of the breccia are variably

509 replaced by fine-grained anhedral feldspar growing at the expense of phyllosilicates.

510   The scheme of Fig. 10 summarizes the inferred depositional sequence in the

511 studied samples. In the scheme the "anomalous" Casargiu HT assemblage is shown

512 separately, because its actual temporal relationships with the other samples are at

513 present unknown.

514

515   5.3 *Mineral chemistry.*

516   In this section, we document the mineral chemistry of major and accessory

517 sulfides and sulfosalts (sphalerite, galena, tetrahedrite, bournonite, pyrargyrite,

518 gersdorffite-ullmannite, pyrite and chalcopyrite) as well as gangue minerals

519 (carbonates). These data complement the mineralogical and textural relationships

520 revealed by microscopic analysis.

521 **Sphalerite** – The compositional data for sphalerite are hosted in Table 5a ESM

522 and Table 6a ESM. The boxplot diagrams in Figures 11a-h summarize the

523 distribution of various major and accessory components measured in selected

524 samples from the different stopes. Iron and cadmium are among the main

525 components. Fe contents clearly distinguish sphalerite from the single Casargiu HT

526 sample sample from all other studied sphalerites. The FeS component in sphalerites

527 from the various Montevecchio veins varies between 0.08 and 8.9 mol% (with

528 average contents between 1.9 and 3.8 mol% FeS), whereas the Casargiu HT dark

529 sphalerite is the most Fe-rich of the whole area: far from chalcopyrite inclusions, FeS

530 contents vary between 5.9 and 18.8 mol%, averaging 14.8 mol% FeS. Microprobe

531 data of sphalerites depict a moderate variability in some elements, revealing a

532 markedly "impure" compositional character. The variability observed for various

533 components also involves single sphalerite crystals displaying more or less regular

534 optical zoning. Various chemical profiles across sphalerite grains shown in Figures 1

535 to 3, Appendix III ESM, document a rather irregular distribution of several accessory

536 components.

537 Cadmium is common in all analysed sphalerites, with no clearcut overall trend

538 and strong variations (from almost Cd-depleted to over 1 wt%). The median and

539 average Cd values, close to and below 0.5 wt% Cd, respectively, appear to be

540 common to all sites. Such Cd values as well as the Cd variability are in agreement

541 with earlier data in bulk sphalerite ores (Table 2 ESM).

542 A feature of the Montevecchio district sphalerites is the rather frequent

543 occurrence of anomalously high Cu and Pb contents (Fig. 11e-f). Occasionally also

544 Ag displays concentrations above the microprobe limit of detection (Fig. 11d). These

545 anomalous Cu, Pb and Ag contents should be ascribed to unrecognized micro-

546 inclusions; we notice however that Montevecchio sphalerite is rather transparent, and

547 micro-inclusions in sphalerite visible by SEM imaging are rather rare. Nickel and

548 cobalt also occur occasionally in concentrations above their microprobe detection

549 limits (Fig. 11g-h). Ni-Co sulfarsenide inclusions were observed in sphalerite;

compositional profiles across sphalerite grains (Figures 1-3, Appendix III ESM, show rather irregular distribution of Ni, Co and also Ag peaks. The x-ray maps of a subhedral, zoned sphalerite crystal in Fig. 3 (appendix III ESM) suggest a rather diffused distribution especially for Ni and Co. Germanium as well occasionally occurs in concentrations above the microprobe detection limit (0.02 wt%). The distribution of Ge depicted in the compositional profiles in appendix III ESM also appears rather irregular. In spite of the uncertainty derived from values often close to the detection limits for various elements, the boxplots suggest some variability in accessory elements within samples derived from the same site or vein system: e.g., the variable Cd and Ag "signatures" in the samples from different stopes of the S. Antonio vein system and the anomalous Ag signature of the sphalerite-only ore from Casargiu-Brassey.

Table 6a ESM contains data on the accessory elements determined by LA-ICP-MS in sphalerite from selected samples of the S. Antonio vein system, Sanna veins and Casargiu HT ore facies. Data for Ga, Ge, In, Ag, Co, Ni, Tl and Mn are shown in the boxplots of Fig. 12a-h. Being limited to a restricted number of samples from surface occurrences, these data are by no means exhaustive of the actual features of sphalerite across the Montevecchio district. These data represent the first attempt to obtain information on accessory components beyond the historical data on bulk ore. Within their limits, the data on accessory elements further contribute in characterizing the chemical "signatures" in sphalerite from samples within the same site. This is, for example, the case for Ga from the S. Antonio vein system, highly enriched in samples from Centrale Minghetti and Levante stopes and almost absent in the coarse-grained quartz-hosted sphalerite in the nearby Cantiere Colombi stope. Germanium is in the 100s ppm range in the S. Antonio vein system but appears to be most concentrated only in the Sanna right-hand vein. Indium is highly enriched in the C. Minghetti sphalerite, which is also relatively enriched in Ag (like Casargiu HT), but rather low in Ge. Nickel is in the ppm range, and relatively more enriched in the Casargiu HT sample, while Co contents are in the 100s ppm range, conformable to

579 the microprobe detection limits, and apparently more enriched in the C. Minghetti

580 and right-hand Sanna vein. The latter sites are also characterized by the highest

581 contents in Tl, which was almost always recorded above its detection limit. The Mn

582 contents in the 1000s ppm range best contribute to distinguish the sample

583 representing Casargiu HT ore facies from the Montevecchio samples, where Mn is in

584 the 10s ppm range and, locally, below detection.

585   Trace element data were employed for obtaining temperature estimates of

586 sphalerite deposition by means of the so-called GGIMFis geothermometer, proposed

587 by Frenzel et al. (2016) (Table 6e ESM; see discussion).

588   **Galena** - Unlike sphalerite, the major element composition of galena is

589 minimally variable. When analysed away from detectable micro-inclusions of other

590 phases, galena displays contents below 0.1 wt%, and often below the microprobe

591 detection limits, for all analysed accessory elements (Table 5d ESM). The systematic

592 absence of Ag and Bi is noteworthy. Single point analyses recording accessory

593 contents for Cu (up to 0.68 wt%), Sb (0,58 wt%), Zn (0,28 wt%) and Cd (0.06-0.18

594 wt%) might derive from the ubiquitous and very abundant micro-inclusions of

595 sulfosalts in galena. Trace element analyses by LA-ICP-MS were performed also on

596 galena, especially in inclusion-rich spots. The data could not be processed, but some

597 representative time-resolved depth profiles of trace elements for galena are displayed,

598 together with those for sphalerite, in Fig. 1 and 2 of appendix IV ESM. Time-

599 resolved depth profiles may help in discriminating signals belonging to elements

600 more or less uniformly distributed from those hosted in occasional micro-inclusions.

601 In this respect, these profiles provide additional information about the nature of the

602 extremely abundant galena-hosted (sub-) micro inclusions rarely amenable for

603 electron probe analysis. Elements showing the most intense signals in galena are

604 represented by Cu and Sb, and frequently Ag and Cd, i.e., tetrahedrite components.

605 The profile for the Casargiu HT galena also displays intense Ag signal as well as Se,

606 almost completely absent in the Montevecchio galenas tested.

607   **Pyrite and chalcopyrite** (Table 5e ESM)- Pyrite occurs as an infrequent

608   accessory in the S. Antonio and Sanna vein systems and in the sphalerite-rich ore in

609   the Casargiu veins, and, in relatively higher amounts, in the Casargiu HT facies. In all

610   occurrences, pyrite displays notable contents of Co (0.1-0.5 wt%) and irregular

611   enrichments in Ni (nil to 1.1 wt%), Zn (nil to 0.4 wt%), Pb (nil to 0.3 wt%) and As

612   (nil to 0.5 wt%), possibly from contamination by nearby phases. Chalcopyrite also

613   displays irregular enrichments in Pb and Zn (rarely over 1 wt%), possibly related to

614   galena and sphalerite hosts, and accessory contents of Co and Ni (rarely above 0.5

615   wt%), not related to As.

616   **Sulfosalts** - As described above, most sulfosalts occur as very small, (sub-)

617   micrometric blebs difficult to analyse, with the exception of coarse fahlore aggregates

618   in samples from Centrale Minghetti stope and Sanna.

619   *Fahlore (tetrahedrite)* - The boxplots in Figs 13 a-h schematize the

620   compositional features of fahlores in the district (see Table 5b ESM). All analyses

621   conform to a general formula $(Cu,Ag)_6Cu_4(Fe,Zn,Cd,Pb)_2(Sb,As)_4S_{13}$ (see George et

622   al., 2017 for a review), with local presence of other minor bivalent metals. We

623   excluded analyses showing a Cu deficit compensated by excess Zn+Fe, most likely

624   suggesting contamination by host sphalerite. In terms of major semimetals, the

625   Montevecchio fahlores cover the whole spectrum between Sb (tetrahedrite s.s.) and

626   As (tennantite) end-members. The compositional range for fahlore is best expressed

627   in the S. Antonio vein system and, particularly, in the Cu-rich ore at Centrale

628   Minghetti stope, where the coarse-grained fahlore aggregates display internal

629   chemical zoning discernible by SEM imaging (Fig. 9c) and even manifested by

630   optical effects. These coarse-zoned aggregates may show gradual to sharp rim-to-

631   core changes from Sb-rich to As-rich compositions or viceversa, suggesting cyclical

632   deposition. Compared to the compositional range in S. Antonio vein system, fahlore

633   in the other mining sites considered display end-member Sb or As compositions (Fig.

634   13a-b). In the case of the few galena-hosted tetrahedrite micro-inclusions amenable to

635   analysis (marked in Table 5b), these appear to be mostly Sb-rich. Silver-rich

636 compositions (Fig. 13d) were recorded only at Sanna (left-hand vein) and Telle, and

637 always correspond to Sb end members. Minor Ag contents (few units wt%) are

638 irregularly recorded also in tetrahedrite blebs in the S. Antonio vein system. In the

639 sphalerite-only ore from the Casargiu-Brassey vein, only one measurable inclusion of

640 As-rich, Ag-poor tetrahedrite was found in Ag-bearing sphalerite (see Table 5a

641 ESM). A remarkable feature of Montevecchio fahlores is the widespread occurrence

642 of Cd-bearing compositions (Fig. 13f). The highest Cd contents recorded are 14.5

643 wt% (corresponding to ~ 2.5 apfu Cd), in fine-grained tetrahedrite inclusions within

644 coarse-grained galena at Centrale Minghetti (see Fig. 6c and 9d-c), similar to the

645 occurrence reported by Pattrick (1978). The coarse galena host is in turn overgrown

646 by later crusts of low-Cd (0.11 wt%) sphalerite and Cd-free, strongly zoned

647 tetrahedrite-tennantite cockades and veins. Cd-rich compositions are occasionally

648 recorded also at Sanna and Telle (up to 3.9 wt% Cd), whereas Montevecchio-Levante

649 fahlores sporadically show detectable Cd contents (Fig. 14e and Table 5b ESM). All

650 Cd-rich compositions belong to Sb-rich, but Ag-poor tetrahedrites (with the

651 exception of a single data point at Sanna), suggesting a marked antipathetic relation

652 between Cd and Ag. Similar to what observed in sphalerite, Ni and Co locally occur

653 in detectable amounts in fahlores, up to over 0.5 wt% for Ni and 0.1 wt% for Co,

654 with no sharp differences among mining sites (Fig. 13g-h).

655 *Bournonite and pyrargyrite* - Only a few bournonite blebs at Centrale Minghetti

656 and a single bleb at S. Antonio-Levante reach dimensions adequate for microprobe

657 analysis (Table 5d ESM). Measured bournonite grains show low As contents (below

658 0.15 wt% As), and very low contents of accessory metals. Pyrargyrite [Ag_3SbS_3] is

659 the only, unfrequent, accessory Ag carrier in the adularia-fluorite-bearing assemblage

660 of the Casargiu HT ore facies, where tetrahedrite is absent. Pyrargyrite occurs as the

661 almost pure Sb end member (As below 0.16 wt%; Table 5f ESM).

662 *Ni-Co-(Fe) sulfarsenides* – SEM imaging reveals the internal compositional

663 variability of most Ni-Co(-Fe) sulfarsenide crystals, which locally grow over minute

664 As-bearing (max 0.5 wt% As) pyrite cores, and are almost always zoned (Fig. 9e-f).

665 Almost all crystals analyzed correspond to gersdorffite, with a minor fraction of the

666 Sb endmember ullmannite, while only one crystal was found with pure ullmannite

667 composition (Table 5c ESM). In the diagrams in Fig. 14a-b the Montevecchio

668 gersdorffites are compared with gersdorffite data from the Southern Arburese Ni-Co-

669 As-rich veins, which display similar compositional trends between As and Sb terms.

670 **Carbonates** - Figure 15a-e illustrates the compositional data for carbonates from the

671 from the Montevecchio sample suite (Table 5g ESM). In the samples examined,

672 carbonates display three distinct compositions, namely siderite, Zn-rich carbonate,

673 and calcite. Siderite and Zn-rich carbonate are dominant in all mining sites, except in

674 the Casargiu HT ore facies, which contains Mn-bearing calcite only. Siderite contains

675 variable amounts of Mg, Mn and Zn. Zinc carbonates range between endmember

676 smithsonite and, most frequently, intermediate compositions with siderite. The latter

677 are recorded in the S. Antonio vein system, at Sanna and Casargiu-Brassey, and

678 correspond to the different growth zones in the ore-stage Zn carbonates predating

679 quartz and sphalerite crystallization, shown in Fig. 9i-k. In the galena-rich, sphalerite-

680 poor veinlets from Gennamari (Fig. 4g), siderite is almost devoid of Zn. Calcite is

681 always low in Zn and Mg; it may contain Fe (max 1 wt% FeO) and Mn, up to 1 wt%

682 MnO in the Casargiu HT ore facies. The computation of CO_2 highlighted a tendency

683 to a total oxide sum substantially less than 100 wt% (Table 5g ESM). Such imbalance

684 is affecting carbonate compositions with a combination of high Zn and Mn contents

685 and is maximum (up to 8.9 wt%) in Zn-rich carbonates. The imbalance may indicate

686 a missing component, possibly water, indicated as H_2O^* in Fig. 15d-e. The imbalance

687 may correspond to compositions approaching hydrozincite or else hydrous Zn- and

688 Mn-bearing varieties similar to sclarite (Grice and Dunn, 1989). The zinciferous

689 siderite (or Fe smithsonite, monhemite) described here is closely comparable with

690 what described by Boni et al. (2003a) and sampled from deep parts of the

691 Montevecchio mine.

692

693 5.6 *Fluid inclusion petrography and microthermometry*

694   In general, material containing suitable fluid inclusions turned out to be scarce

695   in our samples. We were able to analyse inclusions in sphalerite and quartz from the

696   S. Antonio vein system and sphalerite from the Casargiu vein. Dimensions of fluid

697   inclusions vary generally from few μm to 20 μm, and rarely reach 100 μm in

698   sphalerite and 50 μm in quartz. Criteria for distinguishing primary, pseudosecondary

699   and secondary inclusions are listed in Appendix I ESM. On the basis of the phase

700   assemblage observed at room temperature two fluid inclusion types distinguished: i)

701   two-phase (liquid+vapor), liquid-rich, aqueous fluid inclusions (LV) and ii) single-

702   phase (liquid), aqueous fluid inclusions (L). In both sphalerite and quartz L and LV

703   inclusions often coexist within single Fluid Inclusion Assemblages (FIA of Goldstein

704   and Reynolds, 1994) (Fig. 16d-f). In sphalerite, L inclusions are smaller than

705   coexisting LV inclusions, whereas in quartz some L inclusions larger than LV

706   inclusions can occur within the same FIA. In quartz crystals L inclusions can be

707   rather abundant, representing, in some cases, the majority of the fluid inclusions of a

708   single FIA. The absence of a vapor phase in L inclusions likely resulted from failure

709   of bubble nucleation due to metastability processes, which usually characterize

710   aqueous fluid inclusions with very high fluid density (Roedder, 1984; Goldstein and

711   Reynolds, 1994). Indeed, most L inclusions in sphalerite and a limited number of L

712   inclusions in quartz nucleated a vapour bubble when kept at low temperature (ca. −

713   18° C) for seven days.

714   Microthermometric results for LV inclusions are reported in Table 7a ESM and

715   summarized in Table 7b ESM, while homogenization temperature (T_h) and final ice

716   melting temperature (Tm_{ice}) frequency histograms and T_h vs. salinity diagrams for

717   fluid inclusions in quartz and sphalerite are shown in Fig. 17a-f. Since the T_h and

718   Tm_{ice} ranges of fluid inclusions with uncertain origin in sphalerite are exactly similar

719   to those of primary and pseudosecondary inclusions, their data were merged together.

720   The limited data reported by Boni et al. (2009) for fluid inclusions in sphalerite and

721   quartz of the S. Antonio vein system have been also included in Fig. 17 for

722   comparison. Many LV inclusions in quartz (including the originally L inclusions)

723   within a single FIA often showed variable T_h, likely because of necking-down

724   process. Thus, in order to avoid collecting data from inclusions affected by this

725   process, we considered only the data from FIAs in which about 90% of the inclusions

726   display T_h values within 15°C interval, according to the criteria of Goldstein and

727   Reynolds (1994). An exception is represented by fluid inclusions interested by

728   necking-down occurring in distinct growth zones of a single quartz crystal (Fig. 16c-

729   d). For these inclusions we considered the Tm_{ice} in order to evaluate salinity changes

730   during quartz deposition. Necking-down, in fact, does not change the salinity of

731   aqueous inclusions. Therefore, Tm_{ice} measurements from all the examined inclusions

732   were considered. Primary and pseudosecondary LV inclusions in sphalerite showed

733   rather similar Tm_{ice} ranges, comprised between -22.2 and -17.2°C (Tab. 7b ESM),

734   with most of the values between -22 and -20°C (Fig. 17); in secondary inclusions

735   Tm_{ice} ranged from -13.9 to -10.3°C (Tab. 7b ESM). Final melting of hydrohalite

736   (Tm_{hh}) was observed in a single inclusion at -27.2°C, where Tm_{ice} occurred at -

737   22.2°C (Tab. 7a ESM). Because of the small fluid inclusion size, first melting could

738   be observed only in few primary inclusions in sphalerite; it apparently occurred

739   between -48° and -40°C. These observations suggest that the aqueous solution

740   contains divalent cations (likely Ca^{2+}) in addition to NaCl (Shepherd et al., 1985).

741   Salinity computed from Tm_{ice} varies from 20.4 to 23.8 equiv. mass % NaCl for

742   primary/pseudosecondary inclusions, and from 14.3 to 17.6 equiv. mass % NaCl for

743   secondary inclusions. Assuming that the trapped fluid mainly contains dissolved

744   NaCl and $CaCl_2$, their contents in the single fluid inclusion showing hydrohalite

745   melting, computed from Tm_{hh} and Tm_{ice}, are 9.7 and 12.9 mass %, respectively. Thus,

746   the total salinity (NaCl+$CaCl_2$) is 22.6 mass %, i.e. not significantly different from

747   the salinity computed only from Tm_{ice} only (23.9 equiv. mass % NaCl).

748   Primary and pseudosecondary LV inclusions in quartz of IGL-4P sample show a

749   wide range of Tm_{ice} from -24.4 to -10.1°C, corresponding to salinity from 14.0 to

750   25.2 equiv. mass % NaCl; secondary inclusions are characterized by smaller

751   variations of Tm_{ice} (-19.3 to -12.2°C), corresponding to salinity between 16.1 and

752 21.9 equiv. mass % NaCl (Tab. 7b ESM). In the single quartz grain characterized by

753 distinct growth zones (Fig. 16c-d), LV inclusions display a distinct trend of

754 decreasing Tm_{ice} across the growth zones, corresponding to a salinity increase toward

755 the external growth zones (Fig. 16c).

756 First melting could be detected in few inclusions between -47° and -40°C. SEM/EDS

757 analyses on salts precipitated from decrepitated inclusions also indicated that cations

758 present in the fluid include Ca and K in addition to Na. In one secondary inclusion

759 Tm_{hh} (-24°C) could be measured (Tab. 7 ESM). The NaCl and $CaCl_2$ concentrations

760 for this inclusion, computed from Tm_{hh} and Tm_{ice} (-17,7°C), are 13.4 and 6.8 mass %,

761 respectively, corresponding to a bulk salinity of 20.2 mass %.

762 Primary and pseudosecondary inclusions in sphalerite showed T_h values comprised

763 between 80.6 and 128.8°C, with most values in the 90-120°C range (Fig. 17).

764 Secondary inclusions showed T_h between 107.7 and 122.7°C (Tab. 7 ESM).

765 Homogeneization temperatures (T_h) of LV inclusions in quartz of the IGL-4P sample

766 are from 86.6 to 131.7°C, with most values between 100 and 130°C (Tab. 7 ESM,

767 Fig. 17). In quartz of the IGL-4P sample, LV inclusions displayed T_h from 86.6 to

768 131.7°C, with most values between 100 and 130°C (Tab. 7b ESM, Fig. 17).

769 Secondary inclusions are characterized by lower T_h between 57.1 and 74.6°C (Tab.

770 7b ESM).

771 5.7 *Stable isotope data on carbonates*

772 Table 8 ESM reports the isotopic ($\delta^{13}C_{PDB}$ and $\delta^{18}C_{SMOW}$) composition of vein

773 siderite from the S. Antonio vein system (Montevecchio, Levante, C. Colombi, C.

774 Minghetti stopes) and from the Sanna, Casargiu-Brassey and Gennamari veins. In the

775 plot of Fig. 18 the siderite data of the Montevecchio mining district are consistently

776 arranged according to an approximately horizontal array characterized by little

777 variable, slightly negative $\delta^{13}C_{PDB}$ values (between -1.8 and -4.95 per mil), and by

778 $\delta^{18}O_{SMOW}$ values spread over a wider range, between +13.9 and +20.1 per mil.

779

780 **6. Discussion**

781   6.1 *General context*

782 Mineralization in the large Montevecchio district is likely the result of a complex

783 sequence of events, that currently can be only in part documented. However, the

784 textural and chemical characters described here are consistent and compatible with

785 older literature and reports in which features of the mineralization from the deeper

786 parts of the veins were also described. Most of the ore deposition occurred in an

787 active tectonic regime, as documented by the abundance of brecciated textures.

788 Specifically, the occurrence of cockade breccias suggests low rates of cement growth

789 compared to high rates of dilational fault slip (Frenzel and Woodcock, 2014). The

790 complex superposition of mineral textures and moderate variations of mineral

791 chemistry suggest repeated pulses of fluids not necessarily synchronous at the district

792 scale. Given this complex picture, and the partial nature of the available data, we

793 make an attempt to draw some provisional conclusions on the basis of available

794 information, aided by a comparison with similar deposits, notably those belonging to

795 the class of Ag-Pb-Zn veins in clastic metasediments, as established by Beaudoin and

796 Sangster (1992), Lefebure and Church (1996), and Beaudoin et al. (1999). The

797 examples proposed by Beaudoin and Sangster (1992) include the supergiant Coeur

798 d'Alene, Idaho, district, two Canadian districts, and three Central European districts

799 (Harz, Freiberg[1], and Pribram), associated to the Variscan chain. Lattanzi et al.

800 (1994) suggested that also the (much smaller) Bottino deposit in the Apuane Alps

801 (northwestern Tuscany) can be assigned to this class.

802 As detailed in Table 9 ESM, the Montevecchio ores fit well most distinctive criteria

803 indicated by Beaudoin and Sangster (1992). Moreover, Lattanzi et al. (2001, 2008)

804 pointed out that Montevecchio, Coeur d'Alene, and Bottino share a similar

805 environmental signature. We further add that the Bottino deposit is hosted in a

806 Paleozoic basement, which is closely related to the southern Variscan chain, and

---

[1] Among the many deposits of the Freiberg district, we refer here to silver-base metal veins ('kb' and 'eb/eq' ores - Ostendorf et al., 2019 and references therein)

807 specifically to the Sardinian segment (Elter & Pandeli, 2005). At the regional scale,

808 deposits that show similarities with the Montevecchio district (in terms of geological

809 context, mineralization style and mineral assemblages) include the vein systems of

810 Lula-Sos Enattos and Argentiera in NE and NW Sardinia respectively (Salvadori and

811 Zuffardi, 1960; Di Colbertaldo and Omenetto, 1962; Venerandi Pirri, 1992). Brigo et

812 al. (1982) and Boni et al. (1996) pointed out the metallogenic affinities of Sardinia

813 and the French Massif Central, where another part of the southern Variscan chain

814 crops out. With specific reference to Ag-Pb-Zn vein deposits, we mention the

815 deposits of Saint Salvy (Cassard et al., 1994), and Pontgibaud (Marcoux and Picot,

816 1985). Actually, Saint Salvy is a Zn-Ge deposit, and contains little Pb and Ag, but we

817 include it in our evaluation because it is a vein deposit hosted in clastic

818 metasediments, spatially associated with a Variscan intrusion. In agreement with the

819 typical features of the class as defined by Beaudoin and Sangster (1992), gold at

820 Montevecchio is practically absent. Conversely, silver grades (0.06 wt%) are low

821 compared to typical values for this class (0.22 to 0.63 wt% according to Beaudoin

822 and Sangster, 1992). All these vein deposits were, in the past, major producers of

823 silver, lead, and zinc. Currently, the interest for these metals may be low to moderate,

824 but, as demonstrated by the example of Saint Salvy, these historical mining districts

825 may represent an attractive target for "critical metals" such as Ge, Ga and In.

826 Another aspect worthy of mention is the occurrence of Ni-Co minerals. This appears

827 as a distinctive feature of many deposits of the class. Specifically, Ni-Co minerals

828 occur at Sos Enattos (Di Colbertaldo and Omenetto, 1962), Bottino (Benvenuti,

829 1991) and Saint Salvy (Cassard et al., 1994). At Montevecchio, gersdorffite seems to

830 predate most of Pb-Zn phases (Fig. 6d and 9e-f). A similar situation occurs in the Ni-

831 Co-As-Pb-Zn ores of the five-element vein-type deposits located near Gennamari,

832 south of the Arbus intrusion (Dessau, 1936; Naitza et al., 2015; Conte et al., 2016;

833 Moroni et al., 2019). There, the Pb-Zn-Ag assemblages clearly postdate the Ni-Co

834 minerals. At Bottino, Saint Salvy and Sos Enattos, Ni-Co minerals postdate early, and

835 predate late, Pb-Zn minerals.

836

837   6.2 *Mineral chemistry*

838   Textures, mineral assemblages and chemical features of ore minerals from the

839   Montevecchio mining district contribute to reconstructing a polyphasic framework in

840   which this huge mineralizing system may have developed. Mineralized structures in

841   the various mining sites share overall textures and main mineral components (galena,

842   sphalerite, carbonates and quartz), but are distinguished by some differences ranging

843   from notable (variations in mineral assemblage) to subtle (variations in mineral

844   composition). As previously stated, mineral assemblages may vary often within

845   parallel veins in the same vein swarm, as shown from the coupling of sphalerite-

846   dominated versus galena-quartz-dominated veins. Even the copper minerals seem to

847   have preference for specific mineralized structures, e.g., the chalcopyrite-fahlore-rich

848   breccias at the Centrale Minghetti stope. However, the extreme abundance of (sub-)

849   micro-inclusions of Cu sulfosalts in galena from all the Montevecchio-related vein

850   systems suggests that copper is a minor, yet widespread, ore component in the whole

851   district. The sphalerite crystals and aggregates at Montevecchio show a remarkable

852   chemical variability at all scales (from single grains to the entire mining district)

853   highlighted by major and, particularly, accessory elements (Fig. 11 and 12).

854   Several recent papers describe the major and trace element compositional systematics

855   of sphalerite in a variety of ore deposit types (e.g., Cook et al., 2009; Ye et al., 2011;

856   Belissont et al., 2014; Frenzel et al., 2016). Beside iron and cadmium, several other

857   elements may replace Zn in the sphalerite structure, either with the same nominal

858   charge (e.g. Ni, Co, Mn), or according to schemes of coupled substitutions involving

859   mono- to tetravalent cations like Ag, Tl, In, Ge, Ga, Sn (summarized in Cook et al.,

860   2009). Additional analytical work is needed because a relation of some accessory

861   element enrichments (including Ag, Co and Ni) to occurrence of (sub)micro-

862   inclusions in sphalerite cannot be excluded at the moment. The preliminary analyses,

863   however, provide information about some compositional features described in the

864   historical sources, such as the "anomalous" Ag enrichments of sphalerite-rich bulk

865 ores and in the low-grade mixed Pb-Zn ore (still accessible) in the S. Antonio vein

866 system, as well as the detection of an unusual accessory component like Mo

867 (Zuffardi, 1953). As suggested by Cook et al. (2009), such Mo signature could be

868 interpreted as related to the local geology, like, for example, the occurrence of Sn-Mo

869 mineralization associated with the local Variscan intrusions (e.g., Naitza et al., 2017).

870 During this study tin in sphalerite could not be quantified, but according to historical

871 sources (Table 2 ESM) sphalerite ore contained Sn traces (few ppm range). Thallium

872 is recorded in all analyzed sphalerites from Montevecchio, especially in the Centrale

873 Minghetti and Cantiere Sanna, even if rarely exceeding 1 ppm, well below the ranges

874 reported by Cook et al. (2009) for Kuroko and Red Dog deposits. These authors

875 recorded a weak positive correlation between Tl and Ge (relatively enriched at

876 Sanna), while Xiong (2007) suggested that monovalent Tl would contribute to

877 coupled substitution of Zn together with trivalent cations including In (relatively

878 enriched at Centrale Minghetti). Major and trace element data, and in particular Fe

879 and Mn, also contributed to further distinguish Montevecchio-type mineralization

880 from the Casargiu HT ore facies.

881 The most significant application of trace element data of sphalerite is the

882 geotermometer proposed by Frenzel et al. (2016), based on contents of Fe, Mn, Ga,

883 Ge and In (GGIMFis thermometer). The thermometer is based on the PC 1*

884 parameter which involves the above temperature-sensitive components and which

885 strongly correlates with homogeneization temperatures of fluid inclusions according

886 to the expression Tcalc = -(54.4 ± 7.3)∗PC 1* + (208 ±10). Table 6e ESM reports the

887 calculation of temperatures, with Ga, Ge, In and Mn (ppm) by LA-ICP-MS and Fe

888 (wt%) both by EPMA (according to the indications in Frenzel et al., 2016) and by

889 LA-ICP-MS. Table 1 summarizes the values of PC 1* and the resulting ranges of

890 temperatures for the sphalerite of the S. Antonio vein system, for the Sanna veins and

891 for the Casargiu HT ore facies according to both approaches. The sphalerite

892 temperatures obtained further contribute in distinguishing Montevecchio from

893 Casargiu HT ore facies. The latter, with sphalerite temperatures between 280° and

894   330°C, appears to be considerably hotter than the Montevecchio-type ore. Although

895   no geochronological data are available for the moment, the galena-sphalerite-

896   adularia-fluorite ore facies at Casargiu may represent mineralization associated with

897   some Arbus-related quartz-porphyry intersected during mining activity.

898   Fahlore chemistry (Fig. 13a-h) is consistent with established trends from

899   literature (Johnson et al., 1986; George et al., 2017), although a peculiar feature is

900   represented by the occurrence of Cd-bearing terms. Ag-rich terms are comparatively

901   scarce and might explain the paucity of Ag in Montevecchio ores with respect to

902   similar deposits. The most Ag-rich fahlores show the expected affinity with Sb-rich

903   terms (Johnson et al., 1986). Cadmium also shows a preferential association with Sb

904   (in agreement with Kharbish et al., 2007, and Krismer et al., 2011). George et al.

905   (2017) suggest that sphalerite is the preferred Cd host in sulphide assemblages

906   including fahlore: as a matter of fact, at Montevecchio, the most Cd-rich tetrahedrite

907   composition was observed in a specific depositional stage where sphalerite was

908   absent.

909

910   6.3 *Nature of ore-forming fluids*

911   As suggested by textural evidence, our fluid inclusion data represent a late stage of

912   mineralization. Primary and pseudosecondary LV inclusions are characterized by

913   relatively low T_h (81-132°C) and rather high salinities (up to 25.2 equiv. mass %

914   NaCl; Fig. 17e-f). The low first melting temperatures shown by some inclusions,

915   supported by SEM/EDS analyses, suggest that the trapped fluid contains $CaCl_2$ in

916   addition to NaCl. The $CaCl_2/(NaCl+CaCl_2)$ mole fractions for the two inclusions in

917   which both Tm_{hh} and Tm_{ice} could be measured, computed by Steele-MacInnis et al.'s

918   (2010) model, are 0.31 and 0.41. The presence of significant Ca in the fluid trapped

919   in minerals from the Montevecchio-Ingurtosu mining area was also determined

920   through crush-leach analysis (Honisch, 2008). We notice here that this author

921   attempted application of several ionic thermometers (Na-K, Mg-Li, and Na-Li) to

922   fluid leached from crushed inclusions in quartz, calcite, barite, galena, and sphalerite.

923   The resulting temperatures spread over a wide range (100° to 700°C), even if most

924   Na-K temperatures for barite, galena and sphalerite are in the order of 250°-300°C.

925   However, these bulk analyses were not correlated to a detailed textural study of fluid

926   inclusion populations, therefore they likely represent superposition of several fluid

927   events.

928   In general, the features of the examined inclusions (i.e. T_h and Tm_{ice} ranges, and

929   the occurrence of $CaCl_2$ in the fluid) are similar to those of the fluid inclusions

930   trapped in ore and gangue minerals in post-Variscan (i.e. Jurassic-Cretaceous) F-Ba-

931   (Pb-Zn-Ag) deposits in Sardinia and Central-Western Europe (Bauer et al., 2019;

932   Behr et al., 1987; Boni et al., 2002, 2009; Cathelineau et al., 2012; Muchez et al.

933   2005; Munoz et al., 1994; Walter et al., 2016). In particular, among the similarities

934   between the Montevecchio and the Saint Salvy deposit (specifically for the

935   zinciferous M4 stage, Munoz et al., 1994), there are also the data of fluid inclusions

936   of sphalerite. In general, such deposits are usually ascribed to the circulation of

937   Jurassic-Cretaceous relatively low-temperature (usually <150°C), H_2O-NaCl-$CaCl_2$

938   brines. The inferred depth of formation of such deposits is relatively shallow; for

939   example, Bauer et al. (2019) estimated a thickness of 2-3 km for the cover of the

940   Cretaceous F-Ba mineralization of Freiberg (Germany), whereas Cathelineau et al.

941   (2012) suggested that the maximum thickness of the sedimentary pile during the

942   formation of the late Jurassic F-Ba-(Pb-Zn) mineralization of Poitu High (France)

943   was <900 m. Moreover, a relatively low-pressure of trapping (i.e. around 100 bars)

944   was estimated for the trapping of fluid inclusions in sphalerite (M4 stage) at Saint

945   Salvy (Munoz et al., 1994).

946   Assuming that also the late Pb-Zn mineralization at Montevecchio formed at

947   relatively similar shallow depth (low-pressure), we can consider a hydrostatic regime

948   during the circulation of hydrothermal fluid. Thus, pressure-temperature conditions

949   that likely occurred during the deposition of sphalerite and quartz can be evaluated

950   from isochores of LV inclusions and different hydrostatic thermo-barometric

951   gradients reported in P-T diagrams (Fig. 19a-b). The thermal gradients in areas

952 interested by hydrothermal circulation are higher than the "average" thermal gradient

953 (i.e. 25-30°C/km). Therefore, for the examined system we consider three different

954 hydrostatitc thermal gradients: 50°C/km, 100°C/km, and 150°C/km. Isochores were

955 computed for the T_h ranges that include most T_h values of primary and

956 pseudosecondary inclusions in sphalerite (90-120°C) and quartz (100-130°C),

957 considering the mean salinity values of the fluid inclusions. As fluid inclusions were

958 not trapped at boiling condition, their T_h values are a minimum estimate of fluid

959 temperature at trapping. The pressure at T_h (i.e. <2.5 bars) corresponds to the

960 minimum trapping pressure. Possible P-T trapping conditions can be obtained from

961 the intersections of the three different thermal gradients with fluid inclusion isochores

962 (Fig. 19a-b). In general, inclusion trapping temperatures are close to their T_h as the

963 differences beteween these two temperatures are always ≤10°C (Fig. 19a-b).

964 Whereas, trapping pressure ranges for inclusions in sphalerite varies from 50-70 bars,

965 considering the 150°C/km gradient, to 160-230 bars, for the 50°C/km gradient (Fig.

966 19a), which are comparable with the trapping pressure estimated for the inclusions of

967 M4 (zinciferous) stage at Saint Salvy (Munoz et al., 1994). Slightly higher ranges

968 (i.e. 60-80 bars and 185-250 bars) are obtained for inclusions in quartz (Fig. 18b).

969 Considering the minimum and maximum estimated hydrostatic pressure, the

970 corresponding depth range is 500-2300 m. In any case, having no independent

971 constraints on actual thermal gradients during the mineralization, these estimates are

972 just indications of the orders of magnitude.

973   We can compare T_h of fluid inclusions in sphalerite from the S. Antonio vein

974 system with temperatures calculated for this mineral by means of the GGIMFiS

975 thermometer (§ 6.2). In our sample set, the ranges of GGIMFiS temperatures

976 calculated with Fe from EPMA and from LA-ICP-MS analyses (Table 1) show

977 mutual overlaps to a variable extent when considering errors. However, the results

978 obtained by using the EPMA Fe data appear to be more closely comparable with

979 those from the fluid inclusion geothermometry. The sphalerite temperatures obtained

980 are in the range of 111±29 to 117±22 °C at Montevecchio/Levante and 142±24 to

981 145±32 °C at Centrale Minghetti, compared to the T_h ranges of 81-122°C (mean

982 101°C) at Cantiere Colombi/Levante and 89-118°C (mean 106°C) at Centrale

983 Minghetti. Only a limited number of samples could be employed for these

984 preliminary analyses. However, also considering the previously mentioned slight

985 pressure correction to be applied to fluid inclusion T_h, the two sets of values are in

986 excellent agreement.

987   In summary, while we cannot exclude the presence of different fluids, the

988 currently available evidence indicates that at least part of mineralization is associated

989 with low temperature (<150°C), high salinity (>20 equiv. mass % NaCl) fluids.

990 Similar H_2O-NaCl-$CaCl_2$-rich fluids are well documented in post-Variscan

991 mineralizing events in Sardinia and Europe (Boni et al., 2002, 2009; Muchez et al.

992 2005; Cathelineau et al., 2012; Naitza et al., 2017). On the basis of the ionic

993 composition of fluid inclusions, determined by crush-leach method, Boni et al. (2009)

994 suggested that the origin of fluids responsible for the deposition of some post-

995 Variscan mineralization in SW (Iglesiente) and SE (Sarrabus) Sardinia mining

996 districts is mainly from evaporated seawater, with a possible small contribution from

997 halite dissolution.

998   On the other hand, fluid inclusion data at Montevecchio, albeit limited, do not

999 provide evidence of high temperature fluids typical of other Ag-Pb-Zn vein deposits

1000 (Beaudoin and Sangster, 1992; Benvenuti et al., 1992; Bauer et al., 2019). In our

1001 study, the only evidence of high temperatures is given by the GGIMFiS thermometer

1002 for the anomalous Casargiu HT sample (Table 1). As previously pointed out, the

1003 relationships between this sample and the remaining set is unclear. We further notice

1004 that fluids of comparatively low temperature and high salinity do occur at some stage

1005 in several Ag-Pb-Zn deposits, e.g. at Pribram (Zak and Dobes, 1991), in late-stage

1006 quartz at Bottino (Benvenuti et al., 1992), and in Freiberg (Bauer et al., 2019), where,

1007 however, they belong to a much later event with respect to the Ag-Pb-Zn ('kb' and

1008 'eb') mineralization (Ostendorf et al., 2019). Most notably, low temperature, high

1009 salinity fluids quite similar to Montevecchio are documented in the Southern

1010 Arburese Ni-Co-As-Pb-Zn vein system developed along the southern margin of the

1011 Arbus pluton (Moroni et al., 2019), as well as at Silius, SE Sardinia (Boni et al.,

1012 2009), and in the main mineralization stage (defined as M4) at Saint-Salvy, France

1013 (Munoz et al. 1994).

1014   The source(s) of these fluids remain speculative; the low temperatures, high

1015 salinities, and the presence of Ca are all typical features of basinal brines. However,

1016 having no precise constraints on the age of mineralization (see next section), any

1017 reference to a specific paleogeographic context to make hypotheses on possible

1018 sources and flow driving forces remains speculative.

1019   The carbon and oxygen isotope data for the Fe carbonates may further

1020 contribute additional information on the mineralizing process and fluids for the

1021 Montevecchio ore system. The horizontal cloud of the siderite data is characterized

1022 by little variable, slightly negative $\delta^{13}C$ values (-1.8 to -5 permil) and moderate shifts

1023 of the oxygen isotope signatures (14.4-20.3 permil) (Fig. 18). The isotopic

1024 composition ($\delta^{13}C$ at -5.14 and -4.82, $\delta^{18}O$ at 20.39 and 21 permil) of the Fe

1025 smithsonite described by Boni et al. (2003a) falls into this range, which is apart from

1026 the supergene Zn carbonates in the MVT Pb-Zn district of Iglesiente. The

1027 Montevecchio siderites overlap the upper portion of the field of Fe carbonates from

1028 the Southern Arburese Ni-Co-As-Pb-Zn veins (partly emplaced in Silurian black

1029 shales). The mildly negative $\delta^{13}C$ signatures at Montevecchio seem to exclude a

1030 major contribution of organic-derived or of "deep seated" carbon (proposed for other

1031 Ag-Pb-Zn veins: Beaudoin & Sangster, 1992; Benvenuti et al., 1992). Rather, the

1032 signature is suggestive of sedimentary carbonate remobilized by, or equilibrated with

1033 the hydrothermal fluid (cf. Munoz et al., 1994). As a matter of fact, the Montevecchio

1034 siderites plot far apart from carbonates of marine origin but display signatures affine

1035 to the Lower Cambrian limestones hosting the Iglesiente Pb-Zn ores (Boni et al.,

1036 1988) and whose isotopic composition reflect polyphase diagenetic recrystallization

1037 events.

1038   Based on thermometric estimates by the GGIMFis thermometer and by fluid

1039 inclusion data, it is possible to derive an approximate oxygen isotope composition of

1040 the aqueous fluid in equilibrium with Montevecchio siderites (Table 8 ESM). The

1041 resulting $\delta^{18}O$ values range between -3.5 and +4.2 ‰. These values are outside the

1042 restricted oxygen isotope composition of magmatic fluids (+5.5 ÷ +10 ‰; Taylor,

1043 1979) and are compatible with the widely variable oxygen isotope signatures

1044 determined for ore-related brines and, in general, basinal/oil-field brines (Kerrich et

1045 al., 1986; Kesler et al., 1997; Hoefs, 2006 and references therein).

1046

1047   6.4 *Sources of ore components and age constraints*

1048   As previously noted by other authors, lead ore at Montevecchio shows a fairly

1049 consistent Pb isotopic signature, markedly distinct from that of the Iglesiente pre-

1050 Variscan MVT district and interpreted by Boni et al. (1992) as suggestive of a mixed

1051 lead source represented by Variscan intrusion and lower Paleozoic clastic sediments.

1052 Ludwig et al. (1989) interpreted the Pb isotopic signatures of galenas from the

1053 Montevecchio district as virtually all Variscan and magmatic, although based on a

1054 comparison with a single value from a K-feldspar sampled in an undefined granitoid

1055 unit of the Arbus pluton. The Pb isotope plots of Fig. 20 (from data in Table 3a ESM)

1056 may add some detail to this picture. The isotopic signature at Montevecchio is similar

1057 to but does not overlap with the available K-feldspar data for Sardinian late Variscan

1058 intrusions, while some overlap occurs with the very limited data of Ordovician felsic

1059 metavolcanics (porphyroids). The data spread at Montevecchio is quite wide, in

1060 contrast to the very restricted field of ore deposits of SE Sardinia (Pb–Zn–Ag

1061 Sarrabus ores and Monte Ollasteddu and Baccu Locci Au–As ores). According to

1062 Dini et al. (2005) and Boni et al. (2009), in the latter district all deposits might have

1063 tapped lead from a single, homogeneous source (or from a homogenized mixture of

1064 different sources). On the contrary, the Montevecchio data seem rather suggestive of

1065 a mixing trend. Lead from Variscan intrusions and/or Ordovician felsic

1066 metavolcanics may have been involved in the mineralizing event, but these cannot be

1067 the sole sources. The Pb isotopic signature of lead from Montevecchio and other

1068 Sardinian deposits is broadly consistent with the isotopic signature of various

1069 European Variscan ore deposits previously mentioned for comparison regarding

1070 geological context, mineral assemblages as well as stable isotope signature of

1071 carbonates (Fig. 18). Therefore, all these deposits seem to have tapped a continental-

1072 scale lead source with a distinctive isotopic signature, to which the influence of local

1073 sources/processes is superimposed.

1074   With respect to sulfur (Fig. 21), all $\delta^{34}S$ values determined for sulfides by

1075 Jensen and Dessau (1966) were slightly positive (from +1.2 to +8.3 per mil; Table 3b

1076 ESM). This rather restricted range of sulfur isotopic signatures is in sharp contrast

1077 with the highly variable Pb isotopic signatures (Fig. 19) suggestive of a high

1078 heterogeneity of metal sources. Interestingly, a number of galena (gn)-sphalerite (sp)

1079 pairs coexisting in the same hand specimens consistently show $\delta^{34}S(sp) > \delta^{34}S(gn)$, as

1080 required by isotopic equilibrium in coexisting base metal sulfides established at

1081 temperatures over 150°C (Kajiwara & Krouse, 1971; Ohmoto & Rye, 1979;

1082 summarized in Seal II, 2006). If isotope compositions of galena and sphalerite pairs

1083 at Montevecchio represent equilibrium, the observed fractionation would correspond

1084 to temperatures from 122° to 251°C (calculated from the equation reported by Seal II,

1085 2006). Jensen and Dessau (1966) do not specify textural relationships of the two

1086 sulfides in the analyzed samples, and there is no conclusive proof of isotopic

1087 equilibrium. These apparent temperatures are slightly higher than those derived from

1088 fluid inclusion studies (see below), and from the GGIMFiS sphalerite thermometer.

1089 Jensen and Dessau (1966) interpreted their data as indicative of a mixed sulfur source

1090 (hydrothermal-magmatic sulfur plus sedimentary sulfur assimilated from country

1091 rocks). In the absence of specific rock data, this interpretation remains possible, but

1092 not demonstrated. Other previously mentioned Ag-Pb-Zn vein deposits, shown in

1093 Fig. 21 for comparison, typically show negative $\delta^{34}S$ values, with the exception of

1094 Saint-Salvy, where values are comparable to Montevecchio. Beaudoin and Sangster

1095 (1992) notice that sulfur isotopes in Ag-Pb-Zn vein deposits usually reflect the

1096 composition of country rocks and suggest a local source for sulfur.

1097   There is no direct dating of Montevecchio ore minerals. Field evidence, mining

1098 reports and historical bibliographic references (Cavinato and Zuffardi, 1948, Wright,

1099 1939) clearly indicate that mineralization of the Montevecchio, Ingurtosu and

1100 Gennamari vein systems postdates the emplacement of the Arbus intrusion as well as

1101 of its late magmatic dikes, and is therefore younger than 304 Ma. Just south of the

1102 Montevecchio district and of the Arbus pluton, the intrusion, at 289 Ma, of the Monte

1103 Linas monzogranites is associated with several small Sn-Mo(W) and Pb-Zn-

1104 (Ag)+fluorite deposits (Naitza et al., 2017) which affect the same area where the

1105 Southern Arburese Ni-Co-As-Pb-Zn five element vein-type system extends. Recent

1106 studies on the latter (Moroni et al., 2019) reported about the high-salinity, low-

1107 temperature ore fluids, comparable with basinal brines. The intersection relationships

1108 between this extensive low-temperature vein system (> 7 km-long) and some of the

1109 monzogranite-related veins are not well exposed, although the type of fluid recorded

1110 in these veins is difficult to reconcile to a hot crustal environment experiencing two

1111 plutonic intrusions, and related fluid circulation, within a time span of few millions of

1112 years. The Montevecchio vein system does show several affinities with these Ni-Co-

1113 bearing veins south of the Arbus pluton, and especially with their Pb-Zn sulfide-rich

1114 late stage (carrying galena extremely rich in sub-microinclusions of sulfosalts and

1115 accessory Ni-Co and Ag phases) and, above all, ore fluid type. There might be a

1116 genetic connection between the Montevecchio and the Southern Arburese vein

1117 systems emplacing after the Variscan magmatism.

1118   Indeed, the late- to post-Variscan events consequent to the extensional tectonic

1119 phases of the post-orogenic collapse might have lead to large-scale and long-lasting

1120 fluid circulation in Sardinia. In this geological framework, summarized by Naitza et

1121 al., (2015a), a succession of late- to post-Variscan regional-scale fluid flows occurred

1122 across Southern Sardinia, producing, for example, extensive orogenic Au

1123 mineralization in the basement of SE Sardinia (Garbarino et al., 2003; Dini et al.,

1124 2005; Funedda et al., 2018), fluorite-barite and Pb-Zn-Ag sulfide deposition at the

1125 Silius deposit (Boni et al. 2009) and in the "Sarrabus silver lode" district (Cortecci et

1126 al., 1987), as well as the fluids responsible for low-temperature Pb-Zn mineralization

1127 and diffuse post-ore dolomitization in the Iglesiente district, south of Montevecchio

1128 (Boni et al., 2002). Absolute ages for these late events include a 270 Ma age in

1129 southwestern Sardinia (Boni et al., 1999), and a 260 Ma age for gold mineralization

1130 at Monte Ollasteddu in southeastern Sardinia (Dini et al., 2005). However, for the

1131 Sardinian metallogenic framework Boni et al. (2009) suggest the possibility of a

1132 wider time interval (Permian to Triassic) for fluid circulation, either as "expression of

1133 only one, long lasting tectonothermal event" or developing as temporally distinct

1134 pulses.

1135 When considering the geometry of the fracture network hosting the veins along

1136 the whole Montevecchio mining district, with its dilational and strike-slip

1137 components, it may be useful to consider the mechanism of fragmentation affecting

1138 Sardinia during late to post-Variscan time. Such process has been monitored by

1139 means of paleomagnetic analyses of Permian dyke swarms (ranging in age from 298

1140 $\pm$ 5 to 270 $\pm$ 10 Ma) and of intercalated sedimentary and volcanic sequences of late

1141 Paleozoic age (Aubele et al., 2014; Edel et al., 2014; Bachtadse et al., 2018).

1142 According to these studies, after emplacement of the Permian dykes, Sardinia was

1143 fragmented into several crustal blocks that experienced differential relative rotations

1144 along vertical axes. These data substantiate the earlier proposition by Edel et al.

1145 (1981), who attributed large-scale block rotation between northern and southern

1146 Sardinia to a major phase of deformation developing in Late Variscan times. Such

1147 results depict a scenario for Permian Sardinia where complex, large-scale shear

1148 deformation in a late-post-orogenic context may have favored regional-scale

1149 migration and focusing of mineralizing fluids. In this context, a reasonable geo-

1150 structural model may explain the geometry of the Montevecchio vein system as a

1151 result of a regional-scale fluid-focusing tectonic corridor (shear zone system)

1152 interfering with a "rigid" body (intrusion), and creating a large-scale, horsetail-like,

1153 braided vein systems (Fig. 22). Such mechanism might also accommodate the

1154 emplacement of the Southern Arburese vein swarm.

1155

1156   7. **Conclusions**

1157 This study summarizes all the available information and provides new data for the

1158 historical Pb-Zn-Ag district of Montevecchio in SW Sardinia, scarcely studied so far.

1159 Similar to other Ag-Pb-Zn vein deposits, Montevecchio was a major producer of base

1160 metals and silver in the past; currently it may have some interest for "critical metals"

1161 such as Ga, Ge, In.

1162 New field studies and sample collection were necessarily limited to the accessible

1163 portions of the veins, but the new data are remarkably consistent with older studies

1164 and mining reports. Ore textures and mineralogical-chemical features at all scales

1165 document a multistage process of mineralization postdating the local Variscan

1166 magmatism and occurring in a tectonically active regime, likely along a regional-

1167 scale dilational to strike-slip fracture system. The exact age of mineralization is not

1168 constrained, but the late-post-orogenic, large-scale block rotation and shear

1169 deformation affecting Sardinia, documented by rotation of Permian dike swarms,

1170 may represent a favourable mechanism for large-scale migration and focusing of

1171 mineralizing fluids. While the presence of different fluids cannot be excluded, the

1172 new data indicate that the Montevecchio ore system is associated with relatively low

1173 temperature ($\leqq$150°C), high salinity (>20wt% equiv. mass NaCl) fluids analogous to

1174 basinal brines. Similar fluids are well documented in post-Variscan mineralizing

1175 events in Sardinia and Europe. The migrating character of basinal brines is

1176 compatible with the "mixed" Pb isotope signature of the Montevecchio ore; the

1177 Arbus intrusion may have contributed to ore lead, but it cannot be the sole source.

1178 The Montevecchio mineralization shows several affinities both with the "five element

1179 vein-type" Ni-Co-As-Pb-Zn deposits developed south of the Arbus pluton as well as

1180 with the class of Ag-Pb-Zn veins in metasediments as defined by Beaudoin &

1181 Sangster (1992). Specifically, the broad similarity of Pb isotope signatures of the

1182 Montevecchio ores with other Ag-Pb-Zn deposits associated with the Variscan chain

1183 throughout Europe suggests a link with a continental-scale "Variscan lead" source.

1184

1205

1206 **Appendices**

1207 **Electronic Supplementary Material**

1208 **Appendix I**

1209 **Analytical methods**

1210   Quantitative Wavelength Dispersion Spectrometry (WDS) microanalyses of

1211 metallic minerals, carbonates and silicates were performed by means of a JEOL JXA

1212 – 8200 electron probe equipped with five wavelength-dispersive spectrometers at the

1213 Earth Science Department, State University of Milano, Italy. The following elements,

1214 standards, analytical/spectral lines, and monochromators were used: Zn (Zn, Kα,

1215 LIFH), Fe (Fe$_2$SiO$_4$, Kα, LIFH), Cd (Cd, Lα, PET), Cu (Cu, Kα, LIFH), Ag (Ag, Lα,

1216 PET), Ni (NiAs, Kα, LIFH), Co (Co, Kα, LIFH), Ge (Ge, Lα, TAP), Mn (MnCO$_3$,

1217 Kα, LIFH), Pb (PbS, Mα, PET), Sb (Sb, Lα, PET), As (NiAs, Lα, TAP), S (ZnS, Kα,

1218 PET), Ca (grossular, Kα, PET), Mg (forsterite, Kα, TAP). The analytical conditions

1219 for the electron beam were: accelerating voltage 15 kV, beam current 5 nA, beam

1220 diameter 1-2 μm, counting time for each element: 30 seconds on peak and 10 seconds

1221 on background. Elemental concentrations were determined after applying $\varphi(\rho z)$

1222 algorithm and corrections for X-ray fluorescence, absorption, atomic number (Z) and

1223 matrices, and by evaluating spectral interferences. Analyses were performed after

1224 verifying that I_{xstd}/I_{std} was 1.00 ± 0.01 for each element, where I_{xstd} was the intensity

1225 of the analysed standard and I_{std} the intensity of the same standard checked after

1226 calibration for each element. Detection limits for microanalyses in WDS mode for the

1227 analyzed elements are as follows (average, in ppm): Zn (730), Fe (334), Cd (257), Cu

1228 (554), Ag (358), Ni (380), Co (349), Ge (223), Mn (324), Pb (444), Sb (490), As

1229 (450), S (125), Ca (131), Mg (145). For the WDS analyses on carbonates it was not

1230 possible to employ any specific carbonate standard, as recommended by Lane and

1231 Dalton (1994) for better comparing signals deriving from the damage of the

1232 electronic beam onto the carbonate lattice in similar matrices. The damage is

1233 especially evident for calcite, which is, fortunately, a minor phase in most of the

1234 mineralized samples examined. For minimizing the damage effects, a wider beam

1235 size (10 μm, instead of 1 μm) was employed when analyzing carbonates. The CO$_2$

1236 content was determined according to stoichiometry on the basis of cations, because

1237 oxygen was not determined quantitatively. Backscattered electron (BSE) images were

1238 collected by means of the scanning electron microscope included in the same probe

1239 apparatus.

1240

1241   In-situ trace element analyses of sphalerite and galena in selected polished

1242 sections were performed at the GeoHistory Facility of the John de Laeter Centre,

1243 Curtin University, Perth, Western Australia in October 2015. The analysis was

1244 determined by means of a Resonetics RESOlution M-50A-LR incorporating a

1245 Compex 102 excimer laser, coupled to an Agilent 7700s quadrupole ICP-MS. After a

1246 20 s period of background analysis, samples were spot ablated for 40 s at a 7 Hz

1247 repetition rate in an ultrahigh purity He–N_2 atmosphere by using a 33/50μm beam

1248 and laser energy (at the sample surface) of 2.8 J/cm^2. Oxide polyatomic interferences

1249 were minimized by tuning flow rates for a ThO/Th to < 0.5%. The chalcogenide glass

1250 IMER-1 (Ding et al., 2011) was used as the primary reference material (RM), to

1251 calculate elemental concentrations and to correct for instrument drift. A combination

1252 of other 3 RMs (NIST610 – Hinton, 2007; GSD-1G – Jochum et al., 2008; BVHO-

1253 2G – Jochum et al., 2007) was used for further assessing the quality of the analyses.

1254 Data were collected on a total of 20 elements by monitoring the following isotopes:

1255 ^{55}Mn, ^{57}Fe, ^{58}Ni, ^{59}Co, ^{63}Cu, ^{66}Zn, ^{71}Ga, ^{72}Ge, ^{75}As, ^{82}Se, ^{95}Mo, ^{107}Ag, ^{111}Cd, ^{115}In,

1256 ^{121}Sb, ^{182}W, ^{197}Au, ^{205}Tl, ^{208}Pb, ^{209}Bi. Only the mass spectra of sphalerite could be

1257 properly reduced, although the galena spectra could be employed in time-resolved

1258 profile diagrams (in Appendix IV, ESM). Elemental concentrations were calculated

1259 using Iolite 3.4 (Paton et al., 2011), and employing ^{34}S (determined by EPMA) as

1260 internal standard (as recommended in Ding et al., 2011). The Limit of Detections

1261 (LODs) were calculated using the Howell method (Howell et al., 2013) to a 3.3σ

1262 uncertainty level. The reduced data, with the corresponding internal standard error

1263 (2s) and limit of detection, the evaluation of Quality Assurance and Quality Control

1264 (QA/QC) for the analyses and the composition of the standards are reported in Tables

1265 5a-b ESM. Tin concentrations could not be quantified because standard IMER-1 does

1266 not contain Sn. Therefore, indium concentrations could not be corrected for the

1267   isobaric interference of ^{115}In with ^{115}Sn. Concentrations of Sn measured in sphalerite

1268   concentrates (Table 2 ESM) were reported to be very low (few ppm range). It is

1269   likely that the correction would be small and within the error (also according to Cook

1270   et al., 2016). Standard IMER-1 is a "chalcogenide glass", nominally oxygen-free;

1271   hence, these analyses might not be subject to interferences on germanium like

1272 ^{56}Fe+^{16}O $\rightarrow$ ^{72}Ge, as with oxygen-bearing MASS-1 standard.

1273

1274   Fluid inclusions were analysed in sphalerite from Cantiere Colombi (CC-2 sample),

1275   Centrale Minghetti (CM-1 sample) of the S. Antonio vein system, and from the

1276   Casargiu vein system (IGL-3G sample), and in quartz from the Cantiere Levante

1277   (IGL-4P sample) of the S. Antonio vein system. Clusters of primary fluid inclusions,

1278   characterized by a random three-dimensional distribution, were observed within

1279   sphalerite crystals (Fig. 16a). In this mineral, fluid inclusions may local occur along

1280   planar arrays (Fig. 16b). Some of these arrays do not apparently reach the edge of the

1281   crystal and they, therefore, contain pseudosecondary inclusions (Roedder, 1984).

1282   Only in one instance a trail of secondary fluid inclusion intercepting the boundary of

1283   the host grain was observed. In other cases, fluid inclusions are of uncertain origin.

1284   Quartz crystals are often characterized by growth zones defined by fluid inclusions

1285   (Fig. 16c-d-e), which are of primary origin according to Roedder's criteria (1984).

1286   Secondary and pseudosecondary fluid inclusions along trails are also common in

1287   quartz (Fig. 16f). Microthermometric measurements were performed with Linkam

1288   THMSG600 heating-freezing stages at CNR-IGG of Florence. The stages were

1289   calibrated by using pure H_2O with critical density, and mixed H_2O-CO_2 (CO_2: 25

1290   mol%) synthetic fluid inclusions. Accuracy was estimated to be $\pm$ 0.1°C for final ice

1291   melting (Tm_{ice}), and $\pm$1°C for the vapor/liquid homogenization (T_h). In order to avoid

1292   decrepitation and stretching phenomena commonly associated with volume

1293   expansion during ice formation in fluid inclusions characterized by high degree of fill

1294   homogenization temperature measurements of two-phases inclusions preceded ice

1295   melting temperature measurements (Roedder 1984, Goldstein and Reynolds, 1994).

1296 Aqueous fluid salinities (expressed in equiv. mass % NaCl) were generally calculated

1297 from Tm_{ice} and the equation of Bodnar (1993) for the H_2O-NaCl system. Salinities of

1298 inclusions displaying Tm_{ice} lower than the eutectic temperature of the H_2O-NaCl

1299 system were computed by extrapolating the equation of Bodnar (1993) below -

1300 21.1°C. The mass % of NaCl and $CaCl_2$ were calculated by means the model of

1301 Steele-MacInnis et al. (2010) in two inclusions for which it was possible to measure

1302 both Tm_{ice} and the melting temperature of hydrohalite (Tm_{hh}). Fluid inclusion

1303 isochores were computed from the Bodnar and Vityk (1994) data by using the Steele-

1304 MacInnis et al. (2012) spreadsheet. Analyses on salt residues precipitated from

1305 decrepitated inclusions were inspected by a Zeiss EVO scanning electron microscope

1306 equipped with an Oxford EDS at MEMA (Centro di Servizi di Microscopia

1307 Elettronica e Microanalisi) of the University of Florence. This method provides at the

1308 best semi-quantitative data information on the major elements dissolved in the fluids

1309 (Roedder, 1984; Haynes et al., 1988).

1310

1311 Carbon and oxygen isotope analyses of carbonates from Montevecchio were carried

1312 out at the IRMS-stable isotope laboratory at the Department of Earth Sciences, State

1313 University of Milano, Italy. The equipment employed was a ThermoFisher Delta V

1314 Isotope Ratio Mass Spectrometer (IRMS) coupled with a Finnigan 2 gas bench.

1315 Powders were obtained from 23 carbonate-rich chips and micro-drillcores - Ø < 3

1316 mm (drilled from polished slabs). Materials were purified from sulfides, when

1317 present, before pulverization. Quantities of material analyzed varied between 0.25 mg

1318 (pure carbonates) and 0.7 mg (samples with variable fraction of silicates/quartz).

1319 Carbonate reference materials, i.e. international standards 603, NBS-18 and CO-8

1320 and internal reference MAMI (Carrara Marble), were employed for monitoring the

1321 efficiency of the system and the reproducibility of data. The standards employed are

1322 calcite of marine and magmatic origin. Further control was performed by periodical

1323 analysis of additional internal reference materials analyzed in other academic

1324 laboratories. These internal reference materials are represented by hydrothermal

mineral species similar to those analyzed in the samples (siderite) and analyzed by

Cortecci and Frizzo (1993) as well as at the MLR Key Laboratory of Isotope

Geology, Institute of Mineral Deposits in Beijing (China; see Martin et al., 2017).

Powders of samples, international standards and internal reference samples were

placed into borosilicate vials, sealed with butyl rubber septa, and flushed with CO_2 at

70°C for 5 minutes for extracting air. Subsequently pure anhydrous phosphoric acid

was added, and acidification of the powder was performed at 80°C for 12 hours

before the session of isotopic analysis. The high temperature coupled with the small

amount of powder ensures a complete dissolution of refractory carbonates and the

absence of fractionation due to incomplete reaction of refractory carbonate species

before the step of isotopic analysis. For assuring internal precision and

reproducibility, the $\delta^{18}O$ and $\delta^{13}C$ values for each sample were derived from

averaging ten individual measurements. The $\delta^{18}O$ and $\delta^{13}C$ values are reported using

the delta (δ) notation in per mil (‰), relative to Vienna Peedee belemnite (V-PDB)

and Vienna standard mean ocean water (V-SMOW), respectively, with precisions of

0.06 to 0.2‰. Data normalization was performed according to the two-point method

described in Paul et al. (2007) and comparing each "unknown" sample with both

international standards and internal reference material affine to the samples. The

evaluation of the oxygen isotope composition of the aqueous fluid in equilibrium

with ore-related siderites was performed by selecting fractionation equations for

siderite-water pairs (after Carothers et al., 1988 and Zheng, 1999) in the "web stable

isotope fractionation calculator" facility managed by Beaudoin and Therrien at

Université Laval, Québec, Canada (Beaudoin and Therrien, 2004, 2009):

http://www2.ggl.ulaval.ca/cgi-bin/alphadelta/alphadelta.cgi

Appendix II

Supergene alteration in the Montevecchio mine district

Several studies (e.g., Cavinato and Zuffardi, 1948; Zuffardi, 1962; Salvadori and

Zuffardi, 1973) indicate that supergene alteration was widespread, and locally

extensive, within the Montevecchio mine district. In the suite of samples examined in this study, the primary ore mineral assemblage is well preserved. However, in some samples it was possible to observe some textures with secondary minerals related to supergene alteration, best developed on galena. In the examined samples galena tended to be comparatively more altered than associated sphalerite. The latter often appears to be fresh, even when in contact with deeply altered galena. An incipient stage of alteration in galena is characterized by very fine-grained spots and rinds of covellite (related to galena-hosted micro-inclusions) (Fig. 1a). Alteration may culminate with almost complete replacement by secondary cerussite or crystalline anglesite (at Colombi stope; Fig. 1b). The deep weathering often isolates and highlights the coarser inclusions of chalcopyrite, fahlore, sphalerite, less affected by alteration. The relationship between supergene weathering of galena seems to correlate with the density of sulfosalt micro-inclusions observed by means of SEM imaging (e.g., Fig. 9b) rather than fracturing. In the samples inspected, inclusion-poor galena affected by extreme cleavage at Sanna was rather fresh compared to undeformed, massive, inclusion-rich galena elsewhere. Siderite was in general fresh, only locally affected by to reddish and dark-brown alteration to spongy aggregates and coatings of Fe hydro-oxides (goethite). But fractures in siderite, with or without Fe oxidation, are occasionally cemented by thin, late-stage calcite or Zn carbonate veinlets, texturally different from the Zn carbonates intergrown with siderite and quartz shown in Fig. 9i-h.

Appendix III

Compositional profiles across sphalerite grains and aggregates

Examples of compositional zoning in sphalerite grains – The diagrams below are aimed to represent elemental distribution of major (Fe, Cd) and accessory elements (Ni, Co, Ag, Ge, Mn) across sphalerite grains at the scale of the micron to the tens of microns. The electron microprobe data employed for the profiles are indicated as "Line + label of the sample in Table 5a ESM. Figures 1 and 2 display profiles on both

1383 coarse- and fine-grained sphalerite crystals from sphalerite- and galena-rich vein

1384 portions in samples from the S.Antonio vein system, Sanna; Arco di Telle and

1385 Casargiu-Brassey. Figure 3 displays the profiles across the euhedral sphalerite crystal

1386 shown in Fig. 9a, which revealed well developed and broadly concentric zoning in

1387 SEM imaging. The profiles are coupled with x-ray elemental maps of Fe, Cd, Ag, Ni

1388 and Co.

1389 The profiles suggest that the distribution of the considered elements, both major and

1390 accessory, might be highly variable and show that the optical zoning observed in thin

1391 section is also chemical. More or less regular concentric patterns may be deduced

1392 from the Fe and Cd data, but, compatibly with the density of measurements,

1393 elemental enrichments may often appear to occur in narrow to very thin, micron-

1394 sized zones instead of wide bands, represented by isolated spikes, rather than more or

1395 less wavy plateaus in the profiles. The signals of accessory elements, shown in the

1396 profiles as well as listed in the table 5a ESM, may also be related to presence of

1397 micro-inclusions in sphalerite, although crystals are rather transparent and SEM

1398 imaging did not reveal richness of micro-inclusions as in galena. In the profiles many

1399 data of accessory elements are close to or below the EPMA detection; therefore, the

1400 x-ray maps obtained for Ag, Ni and Co in Fig.3, cannot be considered quantitatively.

1401 However, these maps may suggest, at least qualitatively, that sphalerite is host to

1402 these elements (either in lattice or as micro-inclusions).

1403

1404 **Appendix IV**

1405 **Time-resolved profiles for selected trace elements in sphalerite and galena**

1406 The diagrams in Figure 1a-g and 2a-f show time-resolved depth profiles for trace

1407 elements measured in sphalerite and galena by means of LA-ICP-MS analysis.

1408 Each profile is representative for each orebody/ore facies/ vein system sampled

1409 across the whole Montevecchio mining district, including the Casargiu HT ore facies.

1410 Table 6b ESM contains the complete list of LA-ICP-MS elemental signals employed

1411 for the construction of the profile diagrams. The signals (as counts per second, cps)

1412 were collected during a time span of 80 seconds. The quantification as ppm of the

1413 corresponding trace element is given only for the sphalerite signals as only the

1414 sphalerite signals could be properly elaborated.

1415 In the profiles, the signals of the background noise are followed by the curves of the

1416 signals from the mineral phase progressively burned by the laser during the spot

1417 analysis lasting about 45 seconds.

1418 Flat spectra might reflect trace elements evenly distributed and hosted as solid

1419 solution in the lattice of the main phase, or else hosted in abundant micro-inclusions

1420 regularly distributed within the main phase. Irregular, wavy and skewed profiles may

1421 suggest the occurrence of isolated inclusions, irregular zoning across the grain drilled

1422 by laser or else sampling of a nearby grain with different element distribution. The

1423 sphalerite profiles tend to show rather flat and regular spectra for Cd, Fe, Co, Ni, Ag,

1424 In, Cu and Ga. Exceptions are shown by the profiles for Telle and Casargiu HT

1425 sphalerites, characterized by complex microtextural features (e.g., chalcopyrite

1426 disease, micro-inclusions, irregular grains, small size) compared to the other coarse-

1427 grained crystals analyzed.

1428 In the case of the graphics for galena in Fig. 2a-f, the flat profiles observed for

1429 several trace elements might be interpreted in reference to the extreme abundance of

1430 sub-micrometric inclusions, because galena revealed an almost pure composition by

1431 means of EPMA microanalysis in the infrequent inclusion-free crystals (or parts of

1432 crystals). As a matter of fact, the intense and homogeneously flat profiles for Cu, Ag

1433 and Sb invariably point to an overwhelming abundance of sulfosalt inclusions with

1434 fahlore-like composition. Cadmium-rich tetrahedrite was detected as measurable

1435 micro-inclusions in galenas from the S. Antonio vein system (Table 5a ESM).

1436 Cadmium signals of rather high intensity are common to basically all galenas

1437 considered, including the Casargiu and Gennamari HT ore facies. Bismuth signals are

1438 another feature in common between the Casargiu HT and the Montevecchio galenas

1439 from Arco di Telle and Montevecchio/Levante. In the latter orebodies Bi signals

1440 appear to be quite intense. Otherwise galenas from the Casargiu-Gennamari HT

1441 display trace element signals quite different from Montevecchio and marked by

1442 relatively intense Se signals.

1443

1444   References

1445   Aubele K., Bachtadse V., Muttoni G., Ronchi A., 2014. Paleomagnetic data

1446 from Late Paleozoic dykes of Sardinia: evidence for block rotations and implications

1447 for the intra-Pangea megashear system. Geochemistry, Geophysics, Geosystems

1448 Volume 15, Issue 5. doi:10.1002/2014GC005325.

1449   Bachtadse V., Aubele K., Muttoni G., Ronchi A., Kirscher U., Kent D.V., 2018.

1450 New early Permian paleopoles from Sardinia confirm intra-Pangea mobility.

1451 Tectonophysics ,749, 21–34.

1452   Barca, S., Ferretti, A., Massa, P., Serpagli, E., 1992. The Hercynian Arburese

1453 Tectonic Unit of SW Sardinia. New stratigraphic and structural data. Riv. Ital.

1454 Paleont. Strat. 98, 119-136.

1455   Bauer, M.E., Burisch, M., Ostendorf, J., Krause, J., Frenzel, M., Seifert, T.,

1456 Gutzmer, J., 2019. Trace element geochemistry of sphalerite in contrasting

1457 hydrothermal fluid systems of the Freiberg district, Germany: insights from LA-ICP-

1458 MS analysis, near-infrared light microthermometry of sphalerite-hosted fluid

1459 inclusions, and sulfur isotope geochemistry. Mineralium Dep., 54, 237-262.

1460   Beaudoin, G., Leach, D.L., Hofstra, A.H., Seifert, Th., Žák, K., 1999. Silver-

1461 lead-zinc veins: a descriptive model. In: Stanley, C.J. et al. (Eds.), Mineral Deposits:

1462 Processes to Processing. A.A. Balkema, Rotterdam, pp. 923-926.

1463   Beaudoin, G., Sangster, D.F., 1992. A descriptive model for silver-lead-zinc

1464 veins in clastic metasedimentary terranes. Econ. Geol. 87, 1005-1021.

1465   Beaudoin, G., Therrien, P., 2004. The web stable isotope fractionation

1466 calculator. In: Handbook of stable isotope analytical techniques, Volume-I. De Groot,

1467 P.A. (ed.). Elsevier: 1045-1047.

1468   Beaudoin, G., Therrien, P., 2009. The updated web stable isotope fractionation

1469 calculator. In: Handbook of stable isotope analytical techniques, Volume-II. De

1470 Groot, P.A. (ed.). Elsevier: 1120-1122.

1471   Behr, H.J., Horn, E.E., Frentzel-Beyme, K., Reutel, C., 1987. Fluid inclusion

1472 characteristics of the Variscan and post-Variscan mineralizing fuids in the Federal

1473 Republic of Germany. Chem Geol, 61, 273-285.

1474   Belissont, R., Boiron, M.-C., Luais, B., Cathelineau, M., 2014. LA-ICP-MS

1475 analyses of minor and trace elements and bulk Ge isotopes in zoned Ge-rich

1476 sphalerites from the Noailhac – Saint-Salvy deposit (France): Insights into

1477 incorporation mechanisms and ore deposition processes. Geochim. Cosmochim. Acta

1478 126, 518–540.

1479   Benvenuti, M., 1991. Ni-sulphides from Bottino mine (Tuscany, Italy). Eur. J.

1480 Mineral. 3, 79-84.

1481   Benvenuti, M., Cortecci, G., Costagliola, P., Lattanzi, P., Ruggieri, G., Tanelli,

1482 G. (1992): The metamorphic-hosted precious- and base-metal deposits of the Bottino-

1483 Valdicastello region (Apuan Alps, Tuscany): an overview. Acta Vulcanol. 2, 45-54.

1484   Bertolio, S., 1909. Segnalazione di tenori d'oro nelle mineralizzazioni di

1485 Montevecchio. Res. Ass. Min. Sarda 14, 8-9.

1486   Bianchini, A, Salvadori, I, Zuffardi, P., 1960a. Contributo alla conoscenza del

1487 giacimento di Montevecchio; Gli elementi accessori della galena - Nota I[a]: Studio

1488 statistico dei mercantili. Rend. Soc. Mineral. Ital. 16, 179-228.

1489   Bianchini, A., Salvadori, I., Zuffardi, P., 1960b. Contributo alla conoscenza del

1490 giacimento di Montevecchio; Gli elementi accessori della galena - nota IIa: Studio

1491 statistico di campioni prelevati nel giacimento. Rend. Soc. Mineral. Ital. 16, 229-280.

1492   Bianchini, A., Salvadori, I., Zuffardi, P., 1961. Contributo alla conoscenza del

1493 giacimento di Montevecchio; Gli elementi accessori della galena - nota III: seguito

1494 dello studio statistico di campioni prelevati nel giacimento. Res. Ass. Min. Sarda, 65,

1495 13-39.

1496   Binotto, C., Boi, G., Cocco, E., Preite, D., Sitta, S., 1987a: Minerali dalle
1497 miniere di Montevecchio (Sardegna) e da altri giacimenti collegati al granito
1498 dell'Arburese. 1ª Parte. Riv. Mineral. Ital. 10, 65-79.

1499   Binotto, C., Boi, G., Cocco, E., Preite, D., Sitta, S., 1987b: Minerali dalle
1500 miniere di Montevecchio (Sardegna) e da altri giacimenti collegati al granito
1501 dell'Arburese. 2ª Parte. Riv. Mineral. Ital. 10, 113-124.

1502   Binotto, C., Boi, G., Cocco, E., Preite, D., Sitta, S., 1987c: Minerali dalle
1503 miniere di Montevecchio (Sardegna) e da altri giacimenti collegati al granito
1504 dell'Arburese. 3ª Parte. Riv. Mineral. Ital. 10, 177-188.

1505   Binotto, C., Boi, G., Cocco, E., Preite, D., Sitta, S. 1988: Minerali dalle miniere
1506 di Montevecchio (Sardegna) e da altri giacimenti collegati al granito dell'Arburese. 4ª
1507 Parte. Riv. Mineral. Ital. 11, 1-16.

1508   Bodnar R.J. 1993. Revised equation and table for determining the freezing point
1509 depression of H_2O-NaCl solutions. Geochimica et Cosmochimica Acta, 57, 683-684.

1510   Bodnar R.J. and Vityk M.O. 1994. Interpretation of microthermometric data for
1511 H_20-NaCl fluid inclusions. In Fluid Inclusions in Minerals, Methods and
1512 Applications, B. De Vivo and M.L. Frezzotti. eds., pub. by Virginia Tech,
1513 Blacksburg, VA (USA), 117-130.

1514   Boni, M., Balassone, G., Fedele, L., Mondillo, N., 2009. Post-Variscan
1515 hydrothermal activity and ore deposits in southern Sardinia (Italy): selected examples
1516 from Gerrei (Silius Vein System) and the Iglesiente district. Per. Mineral., 78, 19-35.

1517   Boni, M., Balassone, G., Villa, I.M., 1999. Age and evolution of granitoids from
1518 South West Sardinia: genetic links with hydrothermal ore bodies. In Stanley, C.J. et
1519 al. Mineral Deposits: Processes to Processing, Balkema, Rotterdam, pp. 1255-1258.

1520   Boni, M., Iannace, A., Köppel, V., Früh-Green, G., Hansmann, W., 1992. Late
1521 to post-hercynian hydrothermal activity and mineralization in south-west Sardinia
1522 (Italy). Econ. Geol. 87, 2113-2137.

1523   Boni, M., Iannace, A., Balassone, G., 1996. Base metal ores in the Lower

1524 Palaeozoic of South-Western Sardinia. In: D. Sangster (Ed.), Carbonate-hosted lead-

1525 zinc deposits: Society of Economic Geologists Special Publication 4, pp. 18–28.

1526   Boni, M., Iannace, A., Pierre, C., 1988. Stable isotope compositions of Lower

1527 Cambrian Pb-Zn-Ba deposits and their host carbonates, Southwestern Sardinia, Italy.

1528 Chem Geol, 72, 267-282.

1529   Boni, M., Muchez, Ph., Schneider, J., 2002. Post-Variscan multiple fluid flow

1530 and mineralization in Sardinia and the Permo-Mesozoic evolution of Western

1531 Europe. In: Blundell, D.J., Neubauer, F., von Quadt, A. (Eds.), The Timing and

1532 Location of Major Ore Deposits in an Evolving Orogen, Geological Society, London,

1533 Special Publications 204, pp. 199–212.

1534   Boni, M., Gilg, H.A., Aversa, G., Balassone, G., 2003a, The "calamine" of

1535 Soutwest Sardinia: geology, mineralogy and stable isotope geochemistry of

1536 supergene Zn mineralization. Econ. Geol., 98, 731-748.

1537   Boni, M., Stein, H.J., Zimmerman, A., Villa, I.M., 2003b. Re-Os age for

1538 molybdenite from SW Sardinia (Italy): a comparison with 40Ar/39Ar dating of

1539 Variscan granitoids. In: Eliopoulos, D.G. (Ed.), Mineral exploration and sustainable

1540 development. Proceedings 7th Biennial SGA Meeting, Athens, Greece. Volume 1.

1541 Millpress, Rotterdam, pp. 247–250.

1542   Bosi, F., Naitza, S., Skogby, E., Secchi, F., Conte, A.M., Cuccuru, S., Hålenius,

1543 U., De La Rosa, N., Kristiannson, P., Nillson, C., Ros, L., Andreozzi, G.B., 2018.

1544 Late magmatic controls on the origin of schorlitic and foititic tourmalines from late-

1545 Variscan peraluminous granites of the Arbus pluton (SW Sardinia, Italy): crystal-

1546 chemical study and petrological constraints. Lithos, 308-309, 395-411.

1547   Brigo, L., Ferrario, A., Marcello, A., Natale, P., Omenetto, P., Padalino, G.,

1548 Salvadori, I., Tocco, S., Uras, I., Valera, R., Zucchetti, S., Zuffardi, P., 1982. Gîtes

1549 filoniens Pb-Zn-F-Ba de baisse température du domaine varisque d'Italie. Bull.

1550 BRGM, section II, 2, 195-206.

Brusca C., Dessau, G., Jensen, M.L., 1965. L'origine dei giacimenti di zinco e piombo dell'Iglesiente alla luce della composizione isotopica dello zolfo dei loro solfuri. Atti Symposium AMS, Cagliari-Iglesias, Sez. 1 A1, pp. 25-32.

Carmignani, L., Cocozza, T., Gandin, A., Pertusati, P.C., 1986. The Geology of Iglesiente. In: Carmignani, L., Cocozza, T., Ghezzo, C., Pertusati, P.C., Ricci, C.A. (Eds.), Guide book to the Excursion in the Paleozoic basement of Sardinia, IGCP project N.5, Newsletter special issue, pp. 31-49.

Carmignani, L., Carosi, R., Di Pisa, A., Gattiglio, M., Musumeci, G., Oggiano, G., Pertusati, P.C., 1994a. The Hercynian chain in Sardinia. Geodinamica Acta 7, 31-47.

Carmignani, L., Ghezzo, C., Marcello, A., Pertusati, P.C., Pretti, S., Ricci, C.A., Salvadori, I., 1994b. Petrology, geology and ore deposits of the Paleozoic basement of Sardinia. Guide book to the field excursion - B3. 16th General Meeting of the International Mineralogical Association, Pisa.

Carothers, W.W., Adami, L.H., Rosenbauer, R.J., 1988. Experimental oxygen isotope fractionation between siderite-water and phosphoric acid liberated CO2-siderite, Geochim. Cosmochim Acta, 52, p. 2445-2450.

Cassard, D., Chabod, J.C., Marcoux E., Bourgine, B., Castaing, C., Gros, Y., Kosakevitch, A., Moisy, M., Viallefond L., 1994. Mise en place et origine des mineralisations du gisement filonien Zn, Ge, Ag, (Pb, Cd) de Noailhac-Saint-Salvy (Tam, France). Chron. Rech. Min. 514, 3-37.

Cathelineau, M., M.-C. Boiron, S. Fourcade, G. Ruffet, N. Clauer, O. Belcourt, Y. Coulibaly, D. A. Banks, and F. Guillocheau, 2012. A major Late Jurassic fluid event at the basin/basement unconformity in western France: $^{40}Ar/^{39}Ar$ and K–Ar dating, fluid chemistry, and related geodynamic context: Chemical Geology, v. 322–323, p. 99–120.

Cavinato, A., Zuffardi, P., 1948. Geologia della miniera di Montevecchio. In: Notizie sull'industria del piombo e dello zinco in Italia. Volume 1. Montevecchio Società Italiana del piombo e dello zinco, pp. 430-464.

1580   Conte, A.M., Cuccuru, S., Naitza, S., Oggiano, G., Secchi, F., Tocco, S., 2016.

1581 Into the depth of the Arburèse vein system: arsenide-sulfide evolution in the Ni-Co

1582 ores. In: Carmina, B., Pesero, M. (Eds.) Minerals rocks and fluids: alphabet and

1583 words of planet earth. 2nd European Mineralogical Conference, Rimini, Book of

1584 Abstract, p. 601.

1585   Cook, N.J., Ciobanu, C.L., Pring, A., Skinner, W., Shimizu, M., Danyushevsky,

1586 L., Saini-Eidukat, B., Melcher, F., 2009. Trace and minor elements in sphalerite: A

1587 LA-ICPMS study. Geochim. Cosmoch. Acta 73, 4761–4791.

1588   Cortecci, G., Reyes E., Leone G., Turi, B., 1987. Sulfur, oxygen, carbon, and

1589 strontium isotope geochemistry of the Sarrabus-Gerrei mining district, Southeastern

1590 Sardinia, Italy. Econ. Geol. 82, 1592-1610.

1591   Cortecci, G., Frizzo, P., 1993. Origin of siderite deposits from the Lombardy

1592 Valleys, Northern Italy – a carbon, oxygen and strontium isotope study. Chem. Geol.

1593 105, 293–303.

1594   Cuccuru S., Naitza S., Secchi F., Puccini A., Casini L., Pavanetto P., Linnemann

1595 U., Hofmann M., Oggiano G., 2016. Structural and metallogenic map of late

1596 Variscan Arbus Pluton (SW Sardinia, Italy), Journal of Maps 12, 860-865.

1597   De Giudici, G., Wanty, R.B., Podda, F., Kimball, B.A., Verplanck, P.L.,

1598 Lattanzi, P., Cidu, R., Medas, D., 2014. Quantifying Biomineralization of Zinc in the

1599 Rio Naracauli (Sardinia, Italy), Using a Tracer Injection and Synoptic Sampling.

1600 Chem. Geol. 384, 110-119.

1601   Dessau, G., 1935. Appunti sui giacimenti minerari di Gennamari-Ingurtosu.

1602 Boll. Soc. Geol. Ital., 54, 229-240.

1603   Dessau, G. (1936). I minerali dei filoni a nichelio e cobalto dell'Arburese

1604 (Sardegna). Per. Mineral. 7, 21–39.

1605   Di Colbertaldo, D, Omenetto, P., 1962. I filoni piombozinciferi di Sos Enattos

1606 (Sardegna). Mem. Acad. Patavina Sci. Lett. Arti 74, 1-30.

1607   Ding, L., Yang, G., Xia, F., Lenehan, C.E., Qian, G., McFadden, A., Brugger, J.,
1608 Zhang, X., Chen, G., Pring, A., 2011. A LA-ICP-MS sulphide calibration standard
1609 based on a chalcogenide glass. Mineralogical Magazine 75, 279–287.

1610   Dini, A., Di Vincenzo, G., Ruggieri, G., Rayner, J., Lattanzi, P., 2005. Monte
1611 Ollasteddu, a new gold discovery in the Variscan basement of Sardinia (Italy): first
1612 isotopic (40Ar−39Ar, Pb) and fluid inclusion data. Miner. Depos. 40, 337-346.

1613   Edel, J. B., Montigny R., Thuizat R., 1981. Late Paleozoic rotations of Corsica
1614 and Sardinia: New evidence from paleomagnetic and K-Ar studies. Tectonophysics,
1615 79, 201–223.

1616   Edel, J. B., Casini L., Oggiano G., Rossi P., Schulmann K., 2014. Early
1617 Permian 90° clockwise rotation of the Maures–Estérel–Corsica–Sardinia block
1618 confirmed by new palaeomagnetic data and followed by a Triassic 60° clockwise
1619 rotation. From: Schulmann, K., Martínez Catalán, J. R., Lardeaux, J. M., Janoušek,
1620 V. & Oggiano, G. (eds), The Variscan Orogeny: Extent, Timescale and the Formation
1621 of the European Crust. Geological Society, London, Special Publications, 405, 333-
1622 361.

1623   Elter, F., Pandeli, E., 2005. Structural-metamorphic correlations between three
1624 Variscan segments in Southern Europe: Maures Massif (France), Corsica(France)–
1625 Sardinia(Italy), and Northern Appennines (Italy). In: Carosi, R., Dias, R., Iacopini,
1626 D., Rosenbaum, G. (Eds.), The Southern Variscan Belt. Journal of the Virtual
1627 Explorer 19, Electronic Edition vol. 1, pp. 1–20.

1628   Frenzel, M., Woodcock, N.H., 2014. Cockade breccia: product of mineralization
1629 along dilational faults. J Struct Geol, 68, 194-206.

1630   Frenzel, M., Hirsch, T., Gutzmer, J., 2016. Gallium, germanium, indium, and
1631 other trace and minor elements in sphalerite as a function of deposit type — A meta-
1632 analysis. Ore Geol. Rev. 76, 52–78.

1633   Funedda A., Naitza S., Buttau C., Cocco F., Dini A., 2018. Structural Controls
1634 of Ore Mineralization in a Polydeformed Basement: Field Examples from the
1635 Variscan Baccu Locci Shear Zone (SE Sardinia, Italy). Minerals 2018(8):456.

George L., Cook N.J., Ciobanu C.L., 2017. Minor and trace elements in natural tetrahedrite-tennantite: effects on element partitioning among base metal sulphides. Minerals, 7, 17.

Goldstein R. H. and Reynolds T. J. 1994 Systematics of fluid inclusions in diagenetic minerals, SEPM Short Course 31.

Grice, J.D., Dunn, P.J., 1989. Sclarite, a new mineral from Franklino, New Jersey, with essential octahedrally and tetrahedrally coordinated zinc: description and structure refinement. Am. Mineral. 74, 1355-1359.

Haynes, F.M., Sterner, S.M., Bodnar, R.J., 1988. Synthetic fluid inclusions in natural quartz. IV. Chemical analyses of fluid inclusions by SEM/EDA: evaluation of method. Economic Geology 52, 969–977.

Hinton, R.W., 2007. NIST SRM 610, 611 and SRM 612, 613 Multi-Element Glasses: Constraints from Element Abundance Ratios Measured by Microprobe Techniques. Geostandards Newsletter 23, 197–207.

Hoefs, H.J. 2006. Stable isotope geochemistry. Springer Verlag Berlin Heidelberg, pp. 286.

Honisch, M., 2008. PbS-ZnS ore mineralization in SW Sardinia (Ingurtosu-Montevecchio). Fluid inclusions investigations. MsThesis lehrstuhl für Geologie und lagerstättenlehre, Montanistische Universität Leoben (Austria).

Howell, D., Griffin, W.L., Pearson, N.J., Powell, W., Wieland, P., O'Reilly, S.Y., 2013. Trace element partitioning in mixed-habit diamonds. Chemical Geology 355, 134–143.

Jensen, M.L., Dessau, G., 1966. Ore deposits of Southwestern Sardinia and their sulfur isotopes. Econ. Geol. 61, 917-932.

Jochum, K.P., Willbold, M., Raczek, I., Stoll, B., Herwig, K., 2007. Chemical Characterisation of the USGS Reference Glasses GSA-1G, GSC-1G, GSD-1G, GSE-1G, BCR-2G, BHVO-2G and BIR-1G Using EPMA, ID-TIMS, ID-ICP-MS and LA-ICP-MS. Geostandards and Geoanalytical Research 29, 285–302.

Jochum, K.P., Wilson, S.A., Abouchami, W., Amini, M., Chmeleff, J., McDonough, W.F., Raczek, I., Rudnick, R.L., Stoll, B., Tonarini, S., 2008. USGS

1666 GSD-1G: A Geological Reference Glass for in situ Elemental and Isotopic Analysis.

1667 AGU Fall Meeting Abstracts 13, V13A-2095.Johnson N.E., Craig J.R., Rimstidt J.D.,

1668 1986. Compositional trends in tetrahedrite. Canadian Mineralogist, 24, 385-397.

1669 Kerrich, R., Strong, D., Andrews, A., Owsiacki, L., 1986. The silver deposits at

1670 Cobalt and Gowganda, Ontario. III: hydrothermal regimes and source reservoirs—

1671 evidence from H, O, C, and Sr isotopes and fluid inclusions. Can J Earth Sci, 23,

1672 1519–1550.

1673 Kesler, S.E., Vennemann, T.V., Frederickson, C., Breithaup, A., Vazquez, R.,

1674 Furman, F.C., 1997. Hydrogen and oxygen isotope evidence of origin of MVT-

1675 forming brines, southern Appalachians. Geoch Cosmoch Acta, 61, 1513-1523.

1676 Kharbish, S., Götzinger, M., Beran, A., 2007. Compositional variations of

1677 fahlore group minerals from Austria. Austrian J. Earth Sci. 100, 44-52.

1678 Krismer, M., Vavtar, F., Tropper, P., Sartory, B., Kaindl, R., 2011. Mineralogy,

1679 mineral chemistry and petrology of the Ag-bearing Cu-Fe-Pb-Zn sulfide

1680 mineralizations of the Pfundererberg (South Tyrol, Italy). Austrian J. Earth Sci. 104-

1681 1, 36-48.

1682 Lane, S.J., Dalton, J.A., 1994. Electronic microprobe analysis of geological

1683 carbonates. Am. Mineral. 79, 745-749.

1684 Lattanzi, P., Benvenuti, M., Costagliola, P., Tanelli, G., 1994. An overview on

1685 recent research on the metallogeny of Tuscany, with special reference to the Apuane

1686 Alps. Mem. Soc. Geol. It 48, 613-625.

1687 Lattanzi P., Fanfani L., Caboi R., Cidu R., Zuddas P. 2001. Environmental ore

1688 deposit models: insights from Sardinia. In "Proceedings of the 10th Internat. Symp.

1689 on Water-Rock Interaction" -WRI-10, Villasimius - Italy, Cidu R. Ed., A.A.

1690 Balkema, Rotterdam, 1245-1248.

1691 Lattanzi, P., Cidu, R., Da Pelo, S., Podda, F., 2008. Environmental mineralogy

1692 and geochemistry of the Montevecchio-Ingurtosu mining district: Toward a geo-

1693 environmental model for Ag-Pb-Zn veins in metasediments. Rend. Online Soc. Geol.

1694 It. 3, 488-489.

Lefebure, D.V., Church, B.N., 1996. Polymetallic Veins Ag-Pb-Zn+/-Au. In: Selected British Columbia Mineral Deposit Profiles, Volume 2 - Metallic Deposits, Lefebure, D.V., Hõy, T. (Eds.), British Columbia Ministry of Energy of Employment and Investment, Open File 1996-13, pp. 67-70.

Ludwig, K.R., Vollmer, R., Turi, B., Simmons, K.R., Perna, G., 1989. Isotopic constraints on the genesis of base-metal ores in southern and central Sardinia. Eur. J. Mineral. 1, 657-666.

Martin, S., Toffolo, L., Moroni, M., Montorfano, C., Secco, L., Agnini, C., Nimis, P., Tumiati, S., 2017. Siderite deposits in northern Italy: Early Permian to Early Triassic hydrothermalism in the Southern Alps. Lithos 284-285, 276-295.

Marcoux, E., Picot, P., 1985. Les minéralisations de Pontgibaud (Puy de Dôme): une approche par la géochimie isotopique du plomb et les paragenèses. Chron. Rech. Min. 481, 27-38.

Moroni, M., Rossetti, P., Naitza, S., Magnani, L., Ruggieri, G., Aquino, A., Tartarotti, P., Franklin, A., Ferrari, E., Castelli, D., Oggiano, G., Secchi, F., 2019. Factors Controlling Hydrothermal Nickel and Cobalt Mineralization—Some Suggestions from Historical Ore Deposits in Italy. Minerals, 9(7), 429.

Muchez, Ph., Heijlen, W., Banks, D., Blundell, D., Boni, M., Grandia, F., 2005. Extensional tectonics and the timing and formation of basin-hosted deposits in Europe. Ore Geol. Rev. 27, 241–67.

Munoz, M., Boyce, A.J., Corjault-Jade, P., Fallick, A.E., Tollon, F., 1994. Multi-stage fluid inclusion in the Palaeozoic basement-hosted Saint-Salvy ore deposit (NW Montagne Noire, southern France). Appl. Geochem. 9, 609-626.

Naitza, S., Oggiano, G., Cuccuru, S., Casini, L., Puccini, A., Secchi, F., Funedda, A., Tocco, S., 2015a. Structural and magmatic controls on Late Variscan Metallogenesis: evidences from Southern Sardinia (Italy). In: André-Mayer, A.S., Cathelineau, M., Muchez, P.H., Pirard, E., Sindern, S. (Eds.), Mineral Resources in a Sustainable World. Proceedings 13th Biennial SGA Meeting, Nancy, France. 1, pp. 161–164.

Naitza, S., Secchi F., Oggiano G., Cuccuru, S., 2015b. New observations on the Ni-Co ores of the southern Arburèse Variscan district (SW Sardinia, Italy). Geoph. Res. Abs. 17, EGU2015, 12659.

Naitza, S., Conte, A.M., Cuccuru, S., Oggiano, G., Secchi, F., Tecce, F., 2017. A Late Variscan tin province associated to the ilmenite-series granites of the Sardinian Batholith (Italy): The Sn and Mo mineralisation around the Monte Linas ferroan granite. Ore Geol. Rev. 80, 1259–1278.

Orgeval, J.-J., Caron, C., Lancelot, J., Omenetto, P., Gandin, A., Libert, A., Courjault Rad, P., Libert, A., Tollon, F., 2000. Genesis of polymetallic and precious-metal ores in the Western Mediterranean province (Cevennes, France – Sardinia, Italy). Applied Earth Science IMM Transactions, section B 109(2), 77-94.

Ostendorf J., Henjes-Kunst, F., Seifert, T., Gutzmer, J., 2019. Age and genesis of polymetallic veins in the Freiberg district, Germany: constraints from radiogenic isotopes. Mineral Dep, 54, 217-236.

Paton, C., Hellstrom, J., Paul, B., Woodhead, J., Hergt, J., 2011. Iolite: Freeware for the visualisation and processing of mass spectrometric data. J. Anal. Spectrom. 26, 2508-2518.

Pattrick, R.A.D., 1978. Microprobe analyses of cadmium-rich tetrahedrites from Tyndrum, Perthshire, Scotland. Mineral. Mag. 42, 286-288.

Preite, D., Zuanel, A. (2007). Montevecchio: storia, miniere e minerali. Riv. Mineral. Ital, 31, 230-246.

Rimatori, C., 1904. Su alcune blende di Sardegna. Atti B. Accad. d. Lincei, 13, 277-285.

Roedder E. (1984). Fluid inclusions. Mineralogical Society of America, Review in Mineralogy, 12, 640 pp.

Rolandi, G., 1940. L'Industria del piombo e dello zinco nel gruppo Montevecchio. Industria mineraria d'Italia e d'oltremare, 1940, 67-77, 245-256.

Salvadori, I., 1958. Studio geo-minerario della zona di Salaponi (Sardegna Sud-occidentale). Boll. Soc. Geol. It. 77, 91-126.

1753 Salvadori, I., Zuffardi, P., 1960. Il campo filoniano di Sos Enattos (Sardegna).
1754 Res. Ass. Min. Sarda 60, 3-45.

1755 Salvadori, I., Zuffardi, P., 1973. Guida per l'escursione a Montevecchio e
1756 all'Arcuentu. Itinerari geologici, mineralogici e giacimentologici in Sardegna. Ente
1757 Minerario Sardo, 1, 29-44.

1758 Seal, R.R., Cooper, B.J., Craig, J.R., 1985. Anisotropic sphalerite of the
1759 Elmwood-Gordonsville deposits, Tennesse. Can. Mineral. 23, 83-88.

1760 Seal, R.R., 2006. Sulfur Isotope Geochemistry of Sulfide Minerals. Rev.
1761 Mineral. Geochem. 61, 633-677.

1762 Secchi, F.A., Brotzu, P., Callegari, E., 1991. The Arburese igneous body (SW
1763 Sardinia, Italy) - An example of dominant igneous fractionation leading to
1764 peraluminous cordierite-bearing leucogranites as residual melts. Chem. Geol. 92,
1765 213-249.

1766 Sprocati, A.R., Alisi, C., Pinto, V., Montereali, M.R., Marconi, P., Tasso, F.,
1767 Turnau, K., De Giudici, G., Goralska, K., Bevilacqua, M., Marini, F., Cremisini, C.,
1768 2013. Assessment of the applicability of a "toolbox" designed for microbially
1769 assisted phytoremediation: the case study at Ingurtosu mining site (Italy). Environ.
1770 Sci. Pollut. Res. 21, 6939-6951.

1771 Stara, P., Rizzo, R., Tanca, A.G., 1996. Iglesiente-Arburese. Miniere e minerali.
1772 Vol. II. Ente Minerario Sardo-Associazione e Gruppi Mineralogici Italiani, Siena.

1773 Steele-MacInnis, M., Bodnar, R.J. and Naden, J. 2010. Numerical model to
1774 determine the composition of H_2O-NaCl-$CaCl_2$ fluid inclusions based on
1775 microthermometric and microanalytical data. Geochimica et Cosmochimica Acta, 75,
1776 21-40.

1777 Steele-MacInnis M., Lecumberri-Sanchez P., Bodnar R.J. 2012.
1778 HOKIEFLINCS_H_2O-NACL: A Microsoft Excel spreadsheet for interpreting
1779 microthermometric data from fluid inclusions based on the PVTX properties of H_2O-
1780 NaCl. Computers & Geosciences, 49, 334-337.

1781 Stoiber, R.E., 1940. Minor elements in sphalerite. Econ. Geol., 35, 501-519.

Stos-Gale Z., Gale N.H., Houghton J., Speakman R., 1995. Lead isotope data from the Isotrace Laboratory, Oxford: *Archeometry* data base 1, ores from the Western Mediterranean. Archeometry, 37, 407-415.

Taylor, H.P., 1979, Oxygen and hydrogen isotope relations in hydrothermal mineral deposits. In: Geochemistry of hydrothermal mineral deposits. Barnes H.L., ed., John Wiley & Sons, New York, 236-277.

Valera RG, Valera P, Rivoldini A., 2005. Sardinian ore deposits and metals in the Bronze Age. Monographies Instrumentum 90, 43-87.

Venerandi Pirri, I., 1992. Willyamite from the Pb-Zn-Ag-Sb deposit of Argentiera, Nurra, NW Sardinia. Eur. J. Mineral. 4, 395-397.

Walter, B.F., Burisch, M., Markl, G., 2016. Long-term chemical evolution and modification of continental basement brines – a field study from the Schwarzwald, SW Germany. Geofluids, 16, 604–623.

Wanty R.B., Podda F., De Giudici G., Cidu R., Lattanzi P., 2013. Zinc isotope and transition-element dynamics accompanying hydrozincite biomineralization in the Rio Naracauli, Sardinia, Italy. Chemical Geology, 337–338, 1–10.

Wright, C.W., 1939. The Pb-Zn ore deposits and geology of the Arbus area in Sardinia, Italy. Econ. Geol., 34, 82-95.

Xiong, Y., 2007. Hydrothermal thallium mineralization up to 300°C: a thermodynamic approach. Ore Geol. Rev. 32, 291–313.

Ye, L., Cook, N.J., Ciobanu, C.L., Yuping, L., Qian, Z., Tiegeng, L., Wei, G., Yulon, Y., Danyushevskiy, L., 2011. Trace and minor elements in sphalerite from base metal deposits in South China: a LA-ICPMS study. Ore Geol. Rev. 39, 188–217.

Zak, K., Dobes, P., 1991. Stable isotopes and fluid inclusions in hydrothermal deposits: The Příbram ore region. Rozpr. Čs. Akad. Věd., Ř. Mat. Přír. Věd., Academia, Prague.

Zheng, Y.-F., 1999. Oxygen isotope fractionation in carbonate and sulfate minerals. Geochem. Journal, 33, 109-126.

1810   Zuffardi, P., 1948. Il giacimento piombo-zincifero di Montevecchio (Sardegna).

1811   Atti XVIII Congresso Geologico Italiano, Iglesias, 305-319.

1812   Zuffardi, P., 1953. Primi risultati delle ricerche sulle profondità delle

1813   mineralizzazioni e sull'imbasamento granitico di Montevecchio. Res. Ass. Min.

1814   Sarda, 57, 5, 5-36.

1815   Zuffardi, P., 1962. Fenomeni di ricircolazione nel giacimento di Montevecchio e

1816   l'evoluzione in profondità della sua mineralizzazione. Res. Ass. Min. Sarda, 66, 17-

1817   73.

1818

1819

1820 **Figure captions**

1821 Figure 1 a-c – Geological framework of the Montevecchio vein system. (a) General sketch map

1822 showing the distribution of the different complexes of the Variscan basement of Sardinia

1823 (after Cuccuru et al., 2016) and the location of the Arburese area. (b) Simplified geological

1824 scheme of the Arburese area with the Variscan Arbus plutonic complex and its contact

1825 metamorphic aureole, the northern margin of the Monte Linas pluton, the Cambrian-Lower

1826 Ordovician Arburese autochtonous unit, the Upper Ordovician parautochtonous foreland and

1827 the outlines of the Montevecchio vein system and of the Southern Arburese Ni-Co-As bearing

1828 vein system (modified after Moroni et al., 2019). (c) Geological scheme of the Montevecchio

1829 vein system showing the distribution of hydrothermal veins (both peripheral and radial

1830 veins), location of the various mining sites and stopes of the district, of Arbus-related quartz

1831 porphyry dikes and of the sampling sites.

1832 Figure 2a-d – Aerial views of the north-western portion of the Montevecchio mining district

1833 (excerpts from Google Maps). a) General view with morphological evidences of the S. Antonio

1834 vein system and the location of some of the sampling sites located between the Montevecchio

1835 Mine and Arco di Telle mineworks. b) Cantiere Levante and Cantiere Colombi stopes

1836 bounding the Montevecchio mine to the east. c) Old adits and excavations on outcropping

1837 veins near Cantiere Sanna mine. d) Large trench on mineralized veins north of the Arco di

1838 Telle mineworks.

1839 Figure 3 a-e - Views of mining stopes and mineralized outcrops of the Montevecchio vein

1840 system. a) Mineralized structures, outcrops and one of the adits at the stopes of Cantiere

1841 Levante (lower) and Cantiere Colombi (higher). b) View of the highly fractured outcrops of

1842 the Sanna veins (named left-hand and right-hand) showing diverging dip. c) Swarm of braided

1843 veinlets with massive to brecciated sphalerite ore in dark grey metapelites along the margin

1844 of the main vein outcropping at Cantiere Levante. d) view of the large trench exposing galena-

1845 rich mineralization just north of the Arco di Telle mine site. e) Outcrop of a barite-galena-rich

1846 vein portion in the trench north of Arco di Telle.

1847 Figure 4a-h - Macroscopic textures of the mineralization from the Montevecchio mining

1848 district. The sequence of the samples is according to mining site and from NE to SW. a)

1849 S.Antonio vein system: coarse-grained sphalerite-rich cockades in siderite. b) S.Antonio vein

1850 system: aggregates of sphalerite crystals and sphalerite-galena nodules in vein quartz (and

1851 minor barite). c) S.Antonio vein system: peculiar parallel to slightly radiating, elongated,

1852 "lamellar" sphalerite aggregates in vein quartz. d) S.Antonio vein system at Centrale

1853 Minghetti: tetrahedrite-rich clots and veinlets intergrown with coarse siderite and quartz

1854 (left), breccia ore with sphalerite-galena-tetrahedrite aggregates cementing deeply altered

1855 wallrock fragments (right). e) Cantiere Sanna: galena-sphalerite ore with coarse euhedral

1856 galena crystals displaying peculiar satin-like luster and internal fibrous-like structure due to

1857 local deformation of cleavage planes. f) Casargiu – Brassey: breccia ore with nodular

1858 sphalerite (dark brown) plus siderite (yellowish) cementing deeply silicified wallrock

1859 fragments. g) Gennamari vein: contorted galena-only veinlets in slightly oxidized siderite

1860 gangue. h) Casargiu HT: stockwork-like to disseminated sphalerite-galena aggregates in

1861 calcite-fluorite-adularia-quartz gangue cementing deeply altered wallrock fragments. Labels:

1862 sph = sphalerite, gn = galena, ttd = tetrahedrite/fahlore, qtz = quartz, sid = siderite, ba =

1863 barite, w/r = wallrock, cc = calcite, K-feld = adularia, fluor = fluorite.

1864 Figure 5 a-f – Microscopic features of ore minerals in the Montevecchio mining district, part I.

1865 Sample labels are indicated. Observation by transmitted (trans) and reflected (refl) light and

1866 in plane polarized light except for (c) – (a) Optical zoning in markedly transparent, euhedral

1867 sphalerite in coarse siderite groundmass - IGL3G2, trans. (b) Zoned sphalerite and galena

1868 intergrown with quartz- CSD7, trans. (c) Variations in hues of the yellow to orange-brown

1869 internal reflections of transparent sphalerite - CSD6, refl crossed pol. (d) Feeble but

1870 perceivable anisotropy in sphalerite enhancing the internal structure with gemination

1871 (indicated by white arrows) - IGL3G1, refl. (e) Strained galena with subhedral sphalerite

1872 crystals - CSD5, refl. (f) Tetrahedrite and chalcopyrite inclusions in galena – CSD5, refl. Labels

1873 in the photos: sph = sphalerite, gn = galena, ttd = tetrahedrite, cpy = chalcopyrite, sid =

1874 siderite, qtz = quartz.

1875 Figure 6 a-f - Microscopic features of ore minerals in the Montevecchio mining district, part II.

1876 Sample labels are indicated. Observation by reflected light and in plane polarized light. (a)

1877 Tetrahedrite veinlets penetrating along regular galena parting planes + enhanced weathering

1878 of galena extremely enriched in (sub-) micro-inclusions of sulfosalts - CM4, refl. (b) Coarse-

1879 grained tetrahedrite in chalcopyrite and galena-bearing stockwork - CM3b, refl. (c)

1880 Concretionary, rhythmic growths of micro-inclusion-rich galena, chalcopyrite, sphalerite and

1881 fahlore; micro-inclusions in galena are Cd-bearing tetrahedrite and bournonite, while the

1882 external fahlore crust is Cd-poor - CM3A. (d) Euhedral gersdorffite crystals with As-bearing

1883 pyrite cores, tetrahedrite and chalcopyrite blebs in galena - IGL2-1. (e) Droplets of native Sb

1884 associated with tetrahedrite and chalcopyrite in galena - GM3. (f) Sphalerite with well

1885 developed "chalcopyrite disease" texture (involving chalcopyrite, pyrrhotite and galena

1886 micro-blebs), intergrown with galena in adularia-quartz-mica gangue, IGL3P Casargiu HT.

1887 Labels in the photos:, sph = sphalerite, gn = galena, cpy = chalcopyrite, ttd =

1888 tetrahedrite/fahlore, brn = bournonite, grsd = gersdorffite, py = pyrite, po = pyrrhotite, sid =

1889 siderite, qtz = quartz, K-feld = adularia; cc = calcite.

1890 Figure 7 a-h – Microtextural features of gangue minerals and their relationships with ore

1891 minerals in the Montevecchio veins. Sample labels are indicated. Observation by transmitted

1892 light and in plane polarized light except in micro-photos in (a), (c) and (f). (a) Hydrothermally

1893 altered lithic fragments cemented by fibrous quartz and siderite - CM2. (b) Lamellar and fan-

1894 shaped siderite in quartz and sulfides - IGL3-G2. (c) Lace-like texture of skeletal siderite

1895 crystals intergrown with quartz - IGL5-S2. (d) Siderite and quartz overgrown by sphalerite -

1896 CM2. (e) and (f) Ghost textures in quartz associated with elongated aggregates of sphalerite in

1897 the "lamellar" sphalerite ore - CC1. (g) and (h) Ghost textures in host rock: blade-shaped

1898 quartz and quartz-siderite-sulfide aggregates probably replacing original lamellar minerals

1899 (carbonate or barite) disseminated in the fractured, silicified and sericitized wallrock - IGL2-1.

1900 Figure 8 a-b - Microtextural features of gangue minerals and their relationships with ore

1901 minerals in the Casargiu HT ore facies. Observation by transmitted light. (a) Zoned lozenge-

1902 shaped adularia crystals intergrown with sulfides (sphalerite-galena), Casargiu HT - IGL3P;

1903 (b) sulfide aggregates (sphalerite-galena) in calcite-adularia-fluorite gangue, Casargiu HT -

1904 IGL3P.

1905 Figure 9 a-k – Microtextural and microchemical features of Montevecchio ore and gangue

1906 mineral phases observed in SEM backscattered images. (a) Variable, radial to concentric

1907 compositional zoning in euhedral sphalerite, IGL2-A. (b) Galena showing variable distribution

1908 of inclusion-rich and inclusion-poor zones, CSS1B. (c) Zoned tetrahedrite aggregates growing

1909 over galena - lighter zones are richer in Sb and poorer in As than the darker ones - CM3A. (d)

1910 Cd-rich tetrahedrite and bournonite micro-inclusions in galena, CM3A. (e) Hourglass-like

1911 zoning in gersdorffite crystals included in sphalerite and chalcopyrite - IGL2-2. (f) Gersdorffite

1912 rims overgrowing pyrite crystals in quartz gangue - IGL2-1. (g) Gold grain included in

1913 sphalerite - IGL1. (h) Native Sb associated with tetrahedrite in galena - GM3. (i) and (j)

1914 Euhedral siderite crystals showing thin to conspicuous rimming by Zn carbonate before

1915 crystallization of quartz - CM2 and IGL3G. (k) Group of lamellar siderite crystals rimmed with

1916 Zn carbonate and crosscut by sphalerite - IGL3G.

1917 Figure 10 – Scheme of the depositional sequences inferred for ore and gangue mineral phases

1918 of the Montevecchio veins and of the "anomalous" Casargiu HT ore facies.

1919 Figure 11 a-h – Mineral chemistry of sphalerite I – Box-and-whisker plot (boxplot) of EPMA

1920 data regarding major and accessory elements (Zn, Fe, Cd, Ag, Cu, Pb, Ni, Co, as wt%) in

1921 sphalerite from the various vein systems, stopes and ore facies occurring in the Montevecchio

1922   mining district. The number of data Considered for each elaboration is given in brackets. A

1923   dotted line indicating EMPA limit of detection (LOD) for accessory elements is added. A

1924   scheme of the features of the boxplots is graphically shown in the legend of Figure 12.

1925   Figure 12 a-h – Mineral chemistry of sphalerite II – Box-and-whisker plot (boxplot) of LA-ICP-

1926   MS data regarding accessory elements Ga, Ge, In, Ag, Co, Ni, Tl and Mn (as ppm) in sphalerite

1927   from a selection of samples from the S. Antonio vein system, Sanna veins, Telle and Casargiu

1928   HT ore facies. The number of data considered for each elaboration is given in brackets. A

1929   scheme of the features of the boxplots is graphically shown in the legend.

1930   Figure 13 a-g - Mineral chemistry of fahlore - Box-and-whisker plot of major and some

1931   accessory element values (Sb, Ag, Zn, Fe, Cd, Ni, Co, as wt%) in fahlore from the various

1932   orebodies and stopes belonging to the Montevecchio vein system. Explanation of the boxplot

1933   features as in Fig. 12. The number of data considered for each elaboration is given in brackets.

1934   Dotted lines are shown indicating limit of detection for some accessory components.

1935   Figure 14 - Mineral chemistry of Ni-Co sulfarsenides – Combined ternary plots of semimetals

1936   (Sb, As) and major cations Ni, Co, Fe, expressed as atomic%, showing variations in Ni versus

1937   Co and in the gersdorffite versus ullmannite (Sb) component. The shaded fields represent the

1938   compositional variation of Ni-Co sulfarsenides associated with Pb-Zn sulfides in the Southern

1939   Arburese vein system (Moroni et al., 2019

1940   Figure 15a-e – Mineral chemistry of carbonates – a) Ternary plot showing the three main

1941   compositions of carbonates (siderite, Zn carbonate and calcite) occurring in the different

1942   orebodies of the Montevecchio veins and in the Casargiu HT ore facies. b to e) Binary plots (as

1943   wt% oxides) showing the different populations of carbonates in terms of Zn, Fe and Mn

1944   abundances, and the imbalance of the total oxide sums, indicated as H_2O^*. The latter is

1945   interpreted as related to a partially hydrous nature of the Zn-richest carbonate varieties

1946   detected in the Montevecchio veins (see text).

1947   Figure 16 a-f – Photomicrographs of fluid inclusions in sphalerite and quartz (transmitted light,

1948   parallel nicols). a) Cluster of two-phase fluid inclusions in sphalerite with a random distribution

1949   (CC-1 sample). b) Plane of two-phase fluid inclusions in sphalerite (CC-1 sample). c) Collage of

1950   photomicrographs showing different growth zones of a quartz crystal (IGL-4P sample), the

1951   growth direction is from bottom left to top right; salinities (in equiv. mass % NaCl) of two-phase

1952   fluid inclusions analysed within the red circles are also shown. d) Enlargement of the blue

1953   rectangle inset of the previous photomicrograph, most inclusions are single phase except few

1954   two-phase (LV) inclusions. e) Primary two-phase (LV) and single-phase (L) inclusions within a

1955   growth zone (IGL-4P sample), the photomicrograph at high-magnification is the enlargement

1956   of the rectangle inset of the low-magnification photomicrograph. f) Secondary (S) and

1957   pseudosecondary (PS) fluid inclusions in quartz (IGL-4P sample), the photomicrograph at high-

1958   magnification is the enlargement of the rectangle inset of the low-magnification

1959   photomicrograph.

1960   Figure 17 a-f - Frequency histograms of final ice melting temperature (Tm_{ice}) of fluid inclusions

1961   in sphalerite (a) and quartz (b); frequency histograms of homogenization temperature (T_h) of

1962   fluid inclusions in sphalerite (c) and quartz (d); T_h vs. salinity diagrams for fluid inclusions in

1963   sphalerite (e) and quartz (f). * = fluid inclusions data of Boni et al. (2009) for the S. Antonio vein

1964   system.

1965   Figure 18 – Carbon and oxygen isotopic composition of Fe carbonates from the Montevecchio

1966   vein system. Additional fields are included for comparing the Montevecchio data with the

1967   isotopic signatures of: Phanerozoic marine limestones (Hoefs, 2006); Cambrian dolomites and

1968   limestones hosting the Pb-Zn ores of the Iglesiente mining district south of Montevecchio

1969   (Boni et al., 1988), Fe carbonates from the Southern Arburese Ni-Co-As-Pb-Zn vein system in

1970   SW Sardinia (Moroni et al., 2019); several worldwide mining districts/ore deposits sharing

1971   some geological and mineralogical similarities with Montevecchio (i.e. Coeur d'Alène, Keno

1972   Hill, Kokanee, Pribram, and Saint Salvy; Beaudoin & Sangster, 1992; Munoz et al., 1994).

1973   Figure 19 – Pressure – temperature diagrams showing the limiting isochores computed from

1974   the minimum and maximum T_h that includes large part of the T_h of primary and

1975   pseudsecondary inclusions in sphalerite (a) and in quartz (b). The hydrostatic thermo-baric

1976   gradients of 50°C/km, 100°C/km and 150°C/km, and the liquid-vapor (LV) curves for the mean

1977   fluid inclusion salinities are also displayed. The intersections of the thermo-baric gradients

1978   with fluid inclusion isochores indicates the P-T conditions under different thermal regimes.

1979   Figure 20 – Plots of uranogenic ($^{207}Pb/^{204}Pb$) and thorogenic ($^{208}Pb/^{204}Pb$) versus stable

1980   ($^{206}Pb/^{204}Pb$) Pb isotope ratios for the Montevecchio ores (galena), for SW Sardinian ores

1981   (including Pb-Zn MVT ores from Iglesiente), for ore deposits from the SE Sardinia (Pb–Zn–Ag

1982   Sarrabus ores, Monte Ollasteddu and Baccu Locci Au–As ores), and for intrusive rocks in

1983   Southern Sardinia (K-feldspar - Ordovician porphyroids and late Variscan granites). Sources:

1984   Ludwig et al., 1989; Valera et al., 2005; Swainbank et al., 1982; Orgeval et al., 2000; Stos-Gale

1985   et al., 1995; Boni et al., 1992; Dini et al., 2005. Additional Pb isotope contours are shown for

1986   ore districts with which Montevecchio shares some affinities (Saint Salvy, Harz, Freiberg,

1987   Pribram, Bottino and Pontgibaud). Sources for the contours: Marcoux and Picot (1985) for

1988   Pontgibaud, Benvenuti et al. (1992) for Bottino, Beaudoin & Sangster (1992) for Pribram,

1989   Harz and Freiberg, Munoz et al. (1994) for Saint Salvy.

Figure 21 – Plot of $\delta^{34}S$ values determined by Jensen & Dessau (1966) on (coarse- and fine-grained) sphalerite, galena, pyrite and chalcopyrite from the S. Antonio, Sanna and Ingurtosu vein systems of the Montevecchio mining district. The ranges of $\delta^{34}S$ values for sulfides from Saint Salvy (Cassard et al., 1994), Coeur d'Alène, Keno Hill, Kokanee, Harz and Pribram (Beaudoin & Sangster, 1992), Freiberg (Bauer et al., 2019) as well as from the MVT ore district of Iglesiente, SW Sardinia (Jensen & Dessau, 1966) are shown for comparison.

Figure 22 – Structural scheme proposed for the development of the regional-scale fracture system hosting the Montevecchio veins (inspired by the structural model proposed for Saint salvy deposit; modified after Cassard et al., 1994).

Figure captions in Appendices ESM

Fig. 1a-b Appendix II – Textures of supergene alteration of galena and replacement of galena by fine-grained cerussite + covellite (a) and by clear, crystalline anglesite (b). Labels: gn = galena, cer = cerussite, cov = covellite, ang = anglesite, sph = sphalerite, qtz = quartz, sid = siderite, ttd = tetrahedrite.

Fig. 1 Appendix III – Examples of major and accessory elemental profiles across coarse-grained sphalerite crystals from sphalerite-rich portions of the S. Antonio vein system, from Cantiere Sanna and from the Casargiu veins (sample suite IGL3G).

Fig. 2 Appendix III – Examples of major and accessory elemental profiles across fine-grained accessory sphalerite crystals from galena-rich vein portions of the S. Antonio vein system, Cantiere Sanna and Arco di Telle. In the last column two profiles are also shown for anisotropic sphalerite from the Gennamari HT/skarn ore facies.

Fig. 12 – Mineral chemistry of sphalerite IV – Combination of SEM imagery, semi-quantitative elemental x-ray maps for Cd, Fe and In and compositional profiles (quantitative WDS data for Fe, Cd, Ag, Ge, Ni Co and Mn) for an optically and chemically zoned euhedral sphalerite crystal from the S. Antonio vein system.

Fig. 1a-g Appendix IV - Representative time-resolved LA-ICP-MS depth profiles for sphalerite in different vein systems, orebodies and ore facies across the Montevecchio mining district. CPS = counts per second

Fig. 2a-h Appendix IV - Representative time-resolved LA-ICP-MS depth profiles for galena in different vein systems, orebodies and ore facies across the Montevecchio mining district. CPS = counts per second.

Tables (in the text)

Table 1 - Ranges of temperatures (with errors) obtained for sphalerite from the S. Antonio vein system (Montevecchio/Levante and Minghetti stopes), the Sanna vein system and the Casargiu HT ore type by applying the GGIMFis geothermometer by Frenzel et al. (2016). The two sets of temperatures correspond to calculation employing Fe data either from EMPA or from LA-ICP-MS analyses (details in Table 6e ESM).

Tables (Electronic Supplementary Material, ESM)

Table 1a ESM – Synoptic scheme summarizing bibliographic data regarding the basic geological, structural and mineralogical features of the Montevecchio vein system. Information derives from literature and mining reports. Primary and secondary mineral phases are listed by means of mineral abbreviations according to Chace (1956) and Kretz (1983). Minerals in bold are dominant, minerals in brackets are reported as subordinate or scarce.

Table 1b - List of additional known mineral species reported as occurring in the mineralized veins of the Montevecchio-Ingurtosu-Gennamari district. Frequency – C: common, S: subordinate, A: accessory, R: rare.

Table 2 ESM – Representative elemental ratios, tenors of accessory and trace elements and correlation indexes between metal pairs in bulk ores (galena and sphalerite concentrates) determined during mining exploitation at Montevecchio and derived from historical sources.

Table 3a ESM – Compilation of Pb isotope data for Montevecchio galena and for Variscan intrusive rocks (K-feldspar) from literature. Sources of data: 1. Ludwig et al., 1989; 2. Valera et al., 2005; 3. Swainbank et al., 1982; 4. Orgeval et al., 2000; 5. Stos-Gale et al., 1995; 6. Boni et al., 1992; Dini et al., 2005. Sample labels and descriptions as reported in the original papers.

Table 3b ESM – Compilation of S isotope data for Montevecchio sulfides (sphalerite, galena, chalcopyrite, pyrite). Source and details about the samples: Jensen and Dessau (1966).

Table 4 ESM – List of the samples considered for the study, with location, mineral assemblage and methods.

Table 5a ESM - Major element chemistry of sphalerite from ore deposits in the Montevecchio mining district (Montevecchio vein system and Casargiu HT ore facies). Compositional data in wt%.

Table 5b ESM - Major element chemistry of fahlore from the Montevecchio vein system. Compositional data in wt%.

2057   Table 5c ESM - Major element chemistry of Ni-Co sulfarsenide micro-inclusions in galena or in

2058   quartz, Montevecchio vein system. Data in wt% and in at%.

2059   Table 5d ESM - Representative major element chemical analyses of galena (1) and bournonite

2060   (2), Montevecchio vein system. Data in wt%.

2061   Table 5e - Representative major element chemical analyses of chalcopyrite (1) and pyrite (2),

2062   Montevecchio vein system. Data in wt%.

2063   Table 5f ESM - Representative major element chemical analyses of pyrargyrite micro-grains

2064   from the Casargiu HT ore facies. Data in wt%.

2065   Table 5g ESM - Major element chemistry of siderite (1), Zn-rich carbonate (2) and calcite (3)

2066   associated with different ore facies in the Montevecchio mining district and in the Casargiu HT

2067   ore facies. Compositional data in wt%.

2068   Table 6a ESM - LA-ICP-MS trace element data of sphalerite in representative samples from the

2069   Montevecchio veins and from the Casargiu HT ore facies. All data in ppm. Values for internal

2070   standard error (2s) and limit of detection are reported in columns labelled Int2SE and LOD for

2071   each analysis.

2072   Table 6b ESM – Evaluation of Quality Assurance and Quality Control (QA/QC) for the laser

2073   analyses. The composition of the standards (in ppm) is reported below.

2074   Table 6c ESM - Comparison between Fe and Cd composition of sphalerite (from different

2075   locations) determined by electron microprobe (EPMA) with data obtained by LA-ICP-MS.

2076   Table 6d ESM - List of LA-ICP-MS elemental signals (as counts per second, cps) counted during

2077   an 80 sec. time span in sphalerite and galena from selected analyses of samples from S.

2078   Antonio vein system (Montevecchio/Levante, C. Colombi and C. Minghetti stopes), Sanna vein

2079   system, Telle and Casargiu HT, and employed for time-resolved profile graphics. The reduced

2080   trace element data corresponding to the sphalerite profiles shown are hosted in Table 6a.

2081   Table 6e ESM - Application of the GGIMFis geothermometer for sphalerite by Frenzel et al.

2082   (2016). List of the major (Fe) and trace element contents required for calculation of the PC 1*

2083   parameter, for the S. Antonio vein system, Sanna vein system and for the Casargiu HT ore

2084   facies. For each sample considered, a comparison is made between values obtained with Fe

2085   contents from EPMA analyses (as average values, in Part 1) and with Fe contents from LA-

2086   ICPMS analyses (in Part 2).

2087   Table 7a ESM - Microthermometric data and computed salinity of the analysed fluid inclusions.

2088   Abbreviations: F.I.A.: fluid inclusion assemblage, GZ#: growth zone number of the quartz crystal

2089   shown in Fig. 16c, Tm_{hh}: final hydrohalite melting temperature, Tm_{ice}: final ice melting

2090   temperature, T_h: homogenization temperatures, P: primary inclusion, PS: pseudosecondary

2091 inclusion, S: secondary inclusion, n.o.: not observed, *: T_h of fluid inclusions affected by necking-

2092 down, these values were not considered in Table 7b ESM and in Fig. 17d and f.

2093

2094 Table 7b ESM. - Table 7b ESM. - Summary of microthermometric and salinity data for primary

2095 (P) pseudosecondary (PS) and secondary (S) fluid inclusions in sphalerite and quartz samples

2096 from the S. Antonio vein system and Casargiu-Brassey Zn-rich vein deposit. Abbreviations: F.I.:

2097 fluid inclusions, Tm_{hh}: final hydrohalite melting temperature, Tm_{ice}: final ice melting

2098 temperature, T_h: homogenization temperatures, n.o.: not observed. Number of measurementes

2099 are reported within brackets.

2100 Table 8a-b - (a) Carbon and oxygen isotope composition of Fe carbonates from the

2101 Montevecchio veins. (b) Estimates of the oxygen composition of acqueous fluid in equibrium

2102 with ore-related siderite representative of the vein systems considered (fractionation

2103 equations for mineral-water pair after Carothers et al., 1988 and Zheng, 1999) and for the

2104 temperature conditions indicated by the application of the GGIMFis sphalerite thermometer

2105 by Frenzel et al. (2016) and by the fluid inclusion analyses.

2106 Table 9 ESM – Comparison of selected features of the Montevecchio ores with the class of Ag-

2107 Pb-Zn veins as defined by Beaudoin & Sangster (1992).

2108

2109

2110 Table 1 - Ranges of temperatures (with errors) obtained for sphalerite from the S. Antonio

2111 vein system (Montevecchio/Levante and Minghetti stopes), the Sanna vein system and the

2112 Casargiu HT ore type by applying the GGIMFis geothermometer by Frenzel et al. (2016). The

2113 two sets of temperatures correspond to calculation employing Fe data either from EMPA or

2114 from LA-ICP-MS analyses (details in Table 6e ESM).

Location	*GGIMFis temperatures (°C)*	
	Fe from EPMA	Fe from LA-ICP-MS
S.Antonio vein – Montevecchio/Levante	111 ± 29 to 117 ± 22	132.9 ± 29 to 133.1 ± 22
S. Antonio vein system - C. Minghetti	142 ± 24 to 145 ± 32	151 ± 30 to 156 ± 39
C. Sanna (right-hand vein)	139 ± 18 to 141 ± 24	149 ± 18 to 153 ± 23
C. Sanna (left-hand vein)	168 ± 17 to 178 ± 22	173 ± 18 to 185 ± 23
Casargiu HT	279 ± 9 to 323 ± 12	283 ± 10 to 330 ± 13

2115

2116

2117

2118

2119

2120

2121

2122

2123

2124

2125

2126

2127

2128

2129

2130

2131   Highlights

2132

2133   • The Montevecchio-Ingurtosu district was one of the largest Italian Pb-Zn-Ag producers
2134   • New field, microscopic, microchemical, isotopic, and fluid inclusion data were obtained
2135   • The Montevecchio deposit shows several affinities with the class of Ag-Pb-Zn veins in metasediments as
2136   defined by Beaudoin & Sangster (1992)
2137   • Ore textures and mineralogical-chemical features at all scales document a multistage process of
2138   mineralization postdating the emplacement of the 304±4 Ma Arbus pluton, and occurring in a tectonically
2139   active regime.
2140   • The exact age of mineralization is not constrained, although it might be related to regional, large-scale shear
2141   deformation in a late-post-orogenic context
2142   • At least part of the mineralization is associated with relatively low temperature (≦200°C), high salinity
2143   (>20wt% equiv. mass NaCl) fluids analogous to basinal brines

2144

2145

2146

2147

2148